J. Fluid Mech. (2023), *vol*. 954, A38, doi:10.1017/jfm.2022.1027

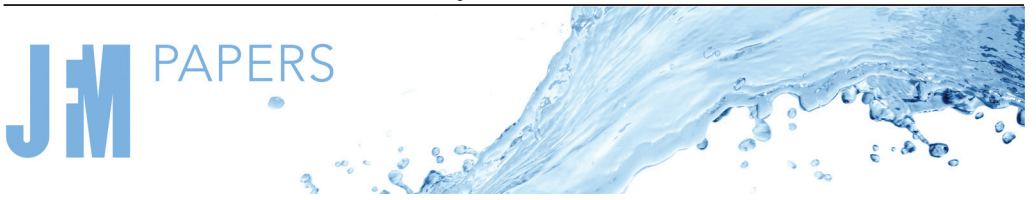

The reduction of pressure losses in thermally modulated vertical channels

J.M. Floryan[1],†, **W. Wang**[1] **and Andrew P. Bassom**[2]

[1]Department of Mechanical and Materials Engineering, The University of Western Ontario, London, Ontario N6A 5B9, Canada

[2]School of Natural Sciences, University of Tasmania, Private Bag 37, Hobart, TAS 7001, Australia

(Received 30 June 2022; revised 12 November 2022; accepted 3 December 2022)

The role played by patterned heating in reducing pressure losses within vertical conduits is investigated. The heating generates flow separation structures which reduce the direct contact between the stream and the sidewalls, thereby limiting the frictional resistance. This also modifies the temperature field thereby inducing a net buoyancy force which may either assist or oppose the pressure gradient required to maintain a fixed flow rate. If the flow Reynolds number is increased sufficiently, the separation structures may be washed away, which means that the pressure-gradient-reducing mechanism is eliminated. The details of the system response are a function of the form of spatial heating distribution, its intensity, the flow Reynolds number and the fluid Prandtl number. Carefully chosen heating of the two walls can induce a pattern interaction effect and a judicious choice of the two patterns can have as much as an order of magnitude effect on the system response.

Key words: reduction of pressure losses, flow control, natural convection, structured convection

1. Introduction

The minimization of pressure losses within conduits is of great interest as otherwise there is likely to be an unnecessary energy cost incurred to maintain the movement of fluid. Such losses stem from one of two main origins: they can be created by the interaction of pressure with the solid walls thereby leading to interaction drag (Mohammadi & Floryan 2012) or arise from the friction between the fluid and the boundaries. Mechanisms that create frictional drag are reasonably well understood but possible strategies to control and reduce this drag are not so advanced. The results presented in this paper provide some general guidance as to how heating patterns might be used to reduce frictional drag.

† Email address for correspondence: floryan@uwo.ca

This is accomplished by encouraging the formation of a net buoyancy force, thereby providing propulsion augmentation in vertical conduits. At face value it might seem that by simply imposing a strong thermal gradient on the slot one could reduce the density of fluid and hence promote the buoyancy effects. Unfortunately, this elementary technique is rarely helpful because the magnitude of the permitted temperature differences is restricted by potential changes in the thermophysical properties of the fluid; this limitation is especially pertinent when the conduit is long. An alternative approach is proposed in this paper where the use of distributed heating patterns with zero mean value is suggested; this eliminates the need for large temperature differences. The resulting thermal field is now known as structured convection (Hossain & Floryan 2013) – a term that is used to reflect the fact that its well-defined topology is controlled by the underlying heating pattern. This convection represents a forced system response which contrasts with the perhaps more familiar Rayleigh–Bénard convection that arises as a bifurcation from the pure conduction state. We point out that there is a well-developed and extensive literature that discusses convection driven by horizontal temperature gradients (Hughes & Griffiths 2008) but this cannot simply be extrapolated to vertical conduits.

Numerous studies of structured convection in horizontal channels have demonstrated conclusively the clear potential for using carefully chosen heating patterns to limit pressure losses (Hossain, Floryan & Floryan 2012; Floryan & Floryan 2015; Hossain & Floryan 2016; Inasawa, Taneda & Floryan 2019). A similar effect can be achieved when looking at the driving force required to maintain the relative movement of parallel plates (Floryan, Shadman & Hossain 2018). This reduction can be achieved whether the heating is applied to the upper or lower wall, or both (Hossain & Floryan 2014, 2015*a*) and results from the formation of flow separation structures that we shall refer to as `bubbles'. These bubbles underpin the operation of three separate effects. First, they reduce the direct contact between the stream and the sidewalls, thus reducing shear; second, the fluid rotates inside the bubbles owing to the heating-induced density gradients and so provides a supplementary propulsion force; and, lastly, the presence of the bubbles restricts the effective flow cross-sectional area which is known to contribute to enhanced pressure losses. The pressure-gradient-reducing effect disappears for excessively fast flows which tend to wash away the separation bubbles. A careful choice of parameter combinations can eliminate the need for a mean pressure gradient to drive the prescribed flow rate owing to heating-induced self-pumping.

The use of patterned heating in horizontal slots leads to interesting theoretical questions regarding the properties of structured convection. This convection commences as steady rolls with a spatial pattern dictated by the heating distribution. An increase in the intensity of heating leads to the formation of secondary states through an instability process that arises owing to a competition between the spatial parametric resonance and the Rayleigh–Bénard mechanism (Bénard 1900; Rayleigh 1916; Hossain & Floryan 2013, 2022). The details of this transition are sensitive to the fluid Prandtl number Pr. Additional complications can arise if the bounding walls are not flat but instead are corrugated as this leads to an interplay between the heating and topography patterns and the activation of this interaction effect (Floryan & Inasawa 2021) leads to the onset of thermal streaming (Abtahi & Floryan 2017*b*, 2018; Inasawa, Hara & Floryan 2021). Topography patterns can create their own convection even when the walls are isothermal; this convection is an example of a forced system response (Abtahi & Floryan 2017*a*). The combination of heating and groove patterns can lead to a reduction in pressure losses greater than that achievable by pure heating alone (Hossain & Floryan 2020). The addition of forced convection can change the nature of the secondary states from stationary rolls to travelling waves (Hossain

& Floryan 2015*b*). It is unclear how this system response might change should the channel be orientated vertically. The limited results concerning natural convection in vertical and oblique channels suggest that a net buoyancy force can be generated even by periodic heating with zero mean and this gives rise to a propulsive force (Floryan, Haq & Panday 2022*b*; Floryan *et al.* 2022*c*).

Heating-modified flows in vertical channels are of importance in various aspects of architectural design as they can affect the performance of heating, ventilation and air conditioning systems. Passive ventilation is achieved through the so-called stack effect, whereby a density difference drives the heated air in the upward direction, thereby drawing in cool air at the base of a structure (Linden 1999; Wong & Heryanto 2004; Mortensen, Walker & Sherman 2011; Nagler 2021). Conversely, in a reverse stack effect hot air is drawn down into a cooler environment. Such systems have performance limitations in terms of the maximum possible flow rate that can be achieved but this can be addressed by adding fans; this has the effect introducing a mean pressure gradient. An appreciation of the properties of flow in vertical channels is also helpful in the design of fire prevention measures in which effective control of the intensification and spreading of combustion is of utmost importance (Song *et al.* 2020). Upright fault lines are found in thermal recovery processes (Tournier, Gethon & Rabinowicz 2000) and in hydraulic fracturing for gas recovery (Gandossi &Von Estorff 2015) with the relevant flows characterized by very small Reynolds numbers. The introduction of pressure gradients can also be used for enhancement of cooling by the chimney effect (Putnam 1882), which has been found to have contemporary applications in the passive cooling of electronic components (Naylor, Floryan & Tarasuk 1991; Straatman, Tarasuk & Floryan 1993; Straatman *et al.* 1994; Novak & Floryan 1995; Shahin & Floryan 1999; Andreozzi, Buonomo & Manca 2005; Mehiris *et al.* 2017) as well as in the design of passively cooled nuclear reactors (Weil 2012). The strength of the chimney effect can be significantly enhanced by using it in conjugation with an externally imposed pressure gradient. We remark that the intriguing concept of a horizontal chimney effect that relies on pattern interaction has been recently proposed (Floryan *et al.* 2022*a*).

It is this plethora of practical applications that motivates the work described below. Here, we focus on the analysis of pressure-gradient-driven flows in vertical channels exposed to patterned heating. It is important to emphasize that our concern is exclusively with laminar flow and the thermal modulation of turbulent flows is outside the scope of our interest. Our starting point is provided by recent study of natural convection in smooth inclined slots exposed to a patterned heating (Floryan *et al.* 2022*b*) which predicts the formation of a net buoyancy force even for purely periodic heating patterns. A study of natural convection in a vertical grooved slot shows the importance of the pattern interaction effect and thermal streaming in such configurations (Floryan *et al.* 2022*c*). In the current work we aim to determine how patterned heating might be used to reduce pressure losses. It is important to emphasize that we confine ourselves to the situation in which the two sides of the vertical channel have equal mean temperatures upon which are superimposed the patterned profiles. Moreover, we restrict ourselves to a study of Boussinesq fluids. In view of the large number of parameters present in the problem, the extension to a non-Boussinesq fluid (Paolucci 1982; Frőhlich, Laure & Peyret 1992), although perfectly possible in theory, would likely lead to a rather opaque and confusing picture. Here, the focus on the role played by the patterning.

The remainder of the paper is organized as follows. In § 2, we introduce our model, which consists of a vertical channel that contains a fluid moving upward together with heating patterns that are applied to the walls. To appreciate some of the properties of the

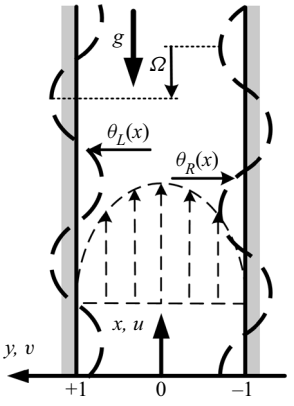

Figure 1. A schematic of the flow system.

flows we perform several computations that are described in §§ 3 and 4. In the first of these we examine the case when only one wall of the conduit is heated and then proceed in § 4 to extend our calculations to allow the heating to be applied to both walls. It is shown that the relative positions of the two heating profiles can have a dramatic effect on the size of the system response. We complement these numerical results with a closer examination of two cases that are amenable to theoretical analysis; in Appendix A we develop the solution structure generated by long-wavelength thermal modulation while the short-wavelength limit is discussed in Appendix B. We round off the paper with a few final remarks and discussion in § 5.

2. Problem formulation

Consider steady two-dimensional pressure-gradient-driven flow of a Boussinesq fluid contained in a vertical isothermal channel formed by two smooth parallel walls unbounded in the x-direction. The sides of the channel are separated by a distance $2h$ and the gravity vector is supposed to act in the negative x-direction, as shown in figure 1. We scale distances on the half-channel width h (so the edges are located at $y = \pm 1$), fluid velocities on the maximum streamwise velocity u_{max} and the pressure on ρu_{max}^2, where ρ denotes the density of the fluid. Then, in the absence of heating, we have the standard forms of the velocity $\boldsymbol{v}_0 = (u_0, v_0)$ and pressure p_0 fields, together with the streamfunction Ψ_0 and the flow rate Q_0 given by

$$\boldsymbol{v}_0(x, y) = (1 - y^2, 0), \quad p_0(x, y) = -2x/Re, \quad \Psi_0 = y - \tfrac{1}{3}y^3 + \tfrac{2}{3}, \quad Q_0 = \tfrac{4}{3}; \tag{2.1a–d}$$

here, the Reynolds number has been defined by $Re = u_{max}h/\nu$, where ν is the kinematic viscosity.

We now apply sinusoidal heating to both walls which means that their (dimensionless) temperatures are

$$y = -1 : \theta_R(x) = \tfrac{1}{2}Ra_{p,R}\cos(\alpha x), \tag{2.2a}$$

$$y = +1 : \theta_L(x) = \tfrac{1}{2}Ra_{p,L}\cos(\alpha x + \Omega); \tag{2.2b}$$

where here, and in what follows, we use the subscripts R and L to describe the properties relating to the right and left walls, respectively. If T denotes the absolute temperature,

then we base the relative temperature θ on the difference $T - T_W$, where T_W is the mean temperature of the walls, and scale it using $\kappa\nu/(g\Gamma h^3)$ as the temperature scale; here, g is the gravitational acceleration, Γ denotes the thermal expansion coefficient and κ is the thermal diffusivity. The intensities of the heating of the walls are described by the two Rayleigh numbers $Ra_{p,R} = g\Gamma h^3 T_{p,R}/(\kappa\nu)$ and $Ra_{p,L} = g\Gamma h^3 T_{p,L}/(\kappa\nu)$; here, $T_{p,L}$ and $T_{p,R}$ are the differences between the maximum and minimum of the left and right periodic temperature components, respectively. We point out that the two thermal profiles (2.2) are perfectly tuned in as much that they are characterized by the same wavenumber α although the two patterns incorporate a phase offset Ω.

Convection in the slot is governed by the scaled continuity, Navier–Stokes and energy equations that can be written as

$$u\frac{\partial u}{\partial x} + v\frac{\partial u}{\partial y} = -\frac{\partial p}{\partial x} + \nabla^2 u + Pr^{-1}\theta, \quad \frac{\partial u}{\partial x} + \frac{\partial v}{\partial y} = 0, \tag{2.3a,b}$$

$$u\frac{\partial v}{\partial x} + v\frac{\partial v}{\partial y} = -\frac{\partial p}{\partial y} + \nabla^2 v, \quad u\frac{\partial \theta}{\partial x} + v\frac{\partial \theta}{\partial y} = Pr^{-1}\nabla^2\theta, \tag{2.3c,d}$$

where (u, v) are the velocity components in the (x, y) directions scaled on $U_v = \nu/h$, p is the pressure scaled with ρU_v^2 and $Pr = \nu/\kappa$ is the Prandtl number. The relevant boundary conditions take the forms

$$u(-1) = u(1) = 0, \quad v(-1) = v(1) = 0, \quad \theta(-1) = \theta_L(x), \quad \theta(1) = \theta_U(x), \tag{2.4a–d}$$

where the functions $\theta_L(x)$ and $\theta_U(x)$ are as defined in (2.2) and the flow fields can be decomposed as

$$u(x, y) = Reu_0(y) + u_1(x, y), \quad v(x, y) = v_1(x, y), \tag{2.5a,b}$$

$$p(x, y) = Re^2 p_0(x) + Bx + p_1(x, y), \quad \psi(x, y) = Re\psi_0(y) + \psi_1(x, y), \tag{2.5c,d}$$

where the subscript 1 refers to modification to the reference flow (2.1) induced by the heating and B denotes the pressure-gradient correction. We are interested in determining whether the imposition of wall heating can lead to a reduction in the pressure gradient required to maintain the specified flow rate. Accordingly, we impose the mass flow rate constraint in the form

$$Q(x)|_{mean} \equiv \lambda^{-1}\int_{x_0}^{x_0+\lambda}\int_{-1}^{1} u(x, y)\,\mathrm{d}y\,\mathrm{d}x = \frac{4}{3}Re, \tag{2.6}$$

where λ is the wavelength of the heating and Q is scaled using U_v. We seek information concerning the mean pressure gradient, i.e.

$$\left.\frac{\partial p}{\partial x}\right|_{mean} \equiv \lambda^{-1}\int_{x_0}^{x_0+\lambda}\frac{\partial p}{\partial x}\,\mathrm{d}x = -2Re + B, \tag{2.7}$$

and remark that positive values of B signify a reduction in the pressure losses.

The system (2.2)–(2.6) was solved by expressing the velocity components using a streamfunction ψ defined in the usual manner, i.e. $u = \partial\psi/\partial y$, $v = -\partial\psi/\partial x$, eliminating pressure and then using Fourier expansions in the x-direction together with Chebyshev expansions in the y-direction. An extensive discussion of the algorithm and the benchmarking of its accuracy have been described elsewhere (Hossain *et al.* 2012) and the reader is referred to that paper for further details. The pressure field was normalized by

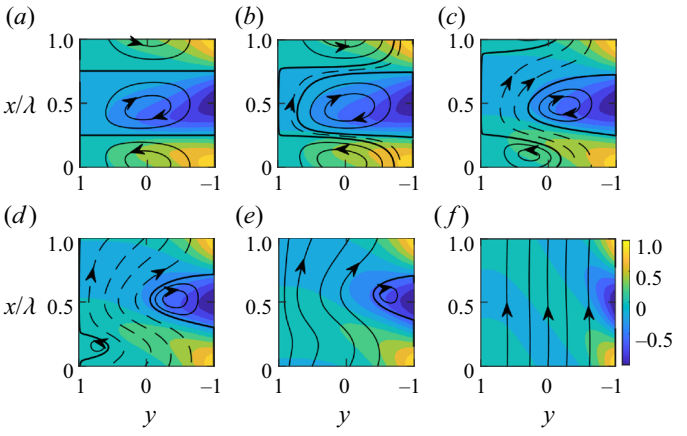

Figure 2. The flow and the temperature fields for one-wall heating with the parameter choices $Ra_{p,R} = 400$, $Pr = 0.71$ and $\alpha = 0.6$. In the sequence of plots the Reynolds number Re is increased from 0 to 100. In (*a*) $Re = 0$, (*b*) 1, (*c*) 5, (*d*) 10, (*e*) 15 and (*f*) 100. In all the plots the temperature has been normalized with its maximum θ_{max}.

bringing the mean value of its periodic component to zero while the mean Nusselt number Nu_{av} was evaluated using

$$Nu_{av} = -\lambda^{-1} \int_{x_0}^{x_0+\lambda} \left. \frac{\partial \theta}{\partial y} \right|_{y=-1} \mathrm{d}x. \tag{2.8}$$

With this definition, positive values of Nu_{av} mean that the right wall losing energy. We remark that the shear forces acting on the fluid at the right and left walls are given by

$$F_R = -\lambda^{-1} \int_0^{\lambda} \left. \frac{\partial u}{\partial y} \right|_{y=-1} \mathrm{d}x, \quad F_L = \lambda^{-1} \int_0^{\lambda} \left. \frac{\partial u}{\partial y} \right|_{y=+1} \mathrm{d}x, \tag{2.9a,b}$$

respectively, while the total (buoyancy) body force per unit length is given by

$$F_b = \lambda^{-1} Pr^{-1} \int_{-1}^{1} \int_0^{\lambda} \theta \, \mathrm{d}x \, \mathrm{d}y. \tag{2.10}$$

3. Heating with an arbitrary wavenumber: one-wall heating

We commence our investigation into the problem by first looking at the case when we restrict the heating to just the right-hand wall ($Ra_{p,L} = 0$); some typical flow patterns are displayed in figure 2. The flow topology for pure natural convection (when $Re = 0$) consists of a family of counter-rotating rolls (figure 2*a*). As the Reynolds number increases the flow pattern can undergo substantial modification. When $Re = 1$ we have a flow field that consists of convection-driven rolls combined with a stream tube that meanders between them and which carries fluid in the positive x-direction (see figure 2*b*). The net upward flow breaks various symmetries present in the natural convection and generates a mean buoyancy force as well as changing the shear forces that act on the two walls. A further increase to $Re = 5$ strengthens the stream tube and shrinks the size of the rolls, which can now be regarded as separation bubbles – the bubbles adjacent to the heated wall are appreciably larger (figure 2*c*). As Re grows yet further this general process continues

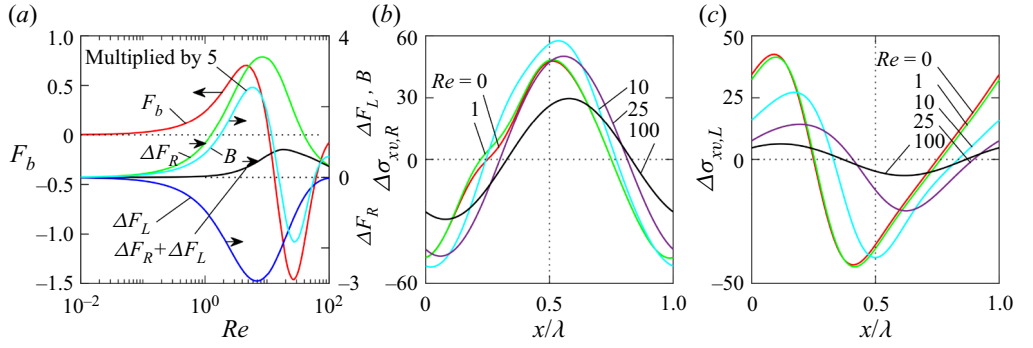

Figure 3. (*a*) The forms of the buoyancy force F_b, the viscous forces differences $\Delta F_R = F_R - F_S$ and $\Delta F_L = F_L - F_S$ at the two walls, the sum $\Delta F_R + \Delta F_L$ and the pressure-gradient correction B as functions of Re. Other parameter values are fixed at values $Ra_{p,R} = 400$, $Pr = 0.71$, $\alpha = 0.6$. (*b*) The distribution of the viscous stress difference $\Delta\sigma_R = \sigma_{xv,R} - \sigma_{xv,S}$ at the right wall and (*c*) the stress difference $\Delta\sigma_L = \sigma_{xv,L} - \sigma_{xv,S}$ at the left wall where $\sigma_{xv,S}$ denotes the shear stress in an isothermal channel. In plots (*b*) and (*c*) five Reynolds numbers are used: $Re = 0$ (red lines), 1 (green), 10 (cyan), 25 (purple), 100 (black).

with the bubbles on the left wall becoming quite small when $Re = 10$ (figure 2*d*); they have completely disappeared by the stage $Re = 15$ (figure 2*e*). In contrast, the bubbles at the right wall persist irrespective of the value of Re and the overall flow becomes essentially rectilinear when $Re = 100$ (figure 2*f*).

Heating-induced rolls tend to decrease the direct contact between the stream and the walls, thereby reducing the frictional resistance. The existence of separation bubbles diminishes the effective flow cross-sectional area, and this typically leads to an increase of pressure losses. The rotational motion of fluid within the bubbles themselves is partially driven by the buoyancy force associated with density variations – this effect provides some propulsion which reduces the pressure drop required to maintain a prescribed flow rate. The mean buoyancy force arises because the net fluid movement destroys symmetries which are present in pure natural convection and whether this force leads to either negative or positive propulsion depends on the flow conditions. The likely cumulative effect is difficult to predict without a careful and detailed analysis.

Figure 3 focuses on the profiles of various forces generated by the heating; in particular, the mean buoyancy force F_b as defined in (2.10) and the forces F_R and F_L (2.9) that act on the right and left walls, respectively. If the values taken by these latter two quantities for the case of an isothermal channel are denoted F_S (note that the isothermal shears on the left and right walls are the same) then it is helpful to examine the differences $\Delta F_R = F_R - F_S$ and $\Delta F_L = F_L - F_S$, the sum $\Delta F_R + \Delta F_L$ together with the pressure-gradient correction B. The data displayed in figure 3(*a*) demonstrate the somewhat intricate role played by F_b for the flow conditions illustrated here. We observe that $F_b = 0$ when $Re = 0$; it then rapidly increases with Re until $Re \approx 5$, which suggests that this force is propelling the fluid. Once Re exceeds approximately 5, F_b decreases and changes sign when $Re \approx 10$; now this buoyancy force opposes the fluid movement. Finally, it reaches a minimum value at $Re \approx 30$ before beginning to grow and becoming positive once more at $Re \approx 60$. The magnitude of the viscous force on the right wall decreases with its maximum value occurring when $Re \approx 10$. Heating always seems to increase the magnitude of the viscous force at the left wall, at least whenever the separation bubbles are present, but the sum of the two wall forces suggests that the overall viscous force is reduced. The pressure-gradient correction correlates well with variations of the mean buoyancy force and the total viscous force for the conditions used in figure 3(*a*). The shear stresses at the

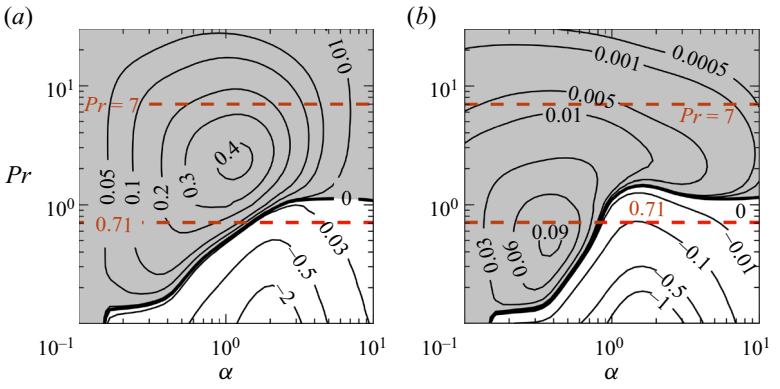

Figure 4. The form of the pressure-gradient correction B/Re as a function of α and Pr when $Ra_{p,R} = 300$ for two values of the Reynolds number; (*a*) $Re = 1$ and (*b*) $Re = 10$. The region of parameter space shaded grey identifies those conditions that correspond to a reduction in the pressure losses.

right wall increase near the hot spots and decrease near the cold spots, as illustrated in figure 3(*b*), with the cumulative effect shown in figure 3(*a*). The qualitative distribution of these stresses along the channel does not change much with Re while the amplitude of their variations decreases as the separation bubbles are reduced and are eventually washed out. Shear stresses at the left wall increase opposite to the hot spots and decrease opposite to the cold spots, as illustrated in figure 3(*c*). Their magnitudes decrease much faster with Re than those at the right wall.

3.1. *The role of the Prandtl number*

The key role played by the mean buoyancy force raises the issue as to the importance of the Prandtl number. Asymptotic analysis presented later in the paper suggests that long-wavelength heating always reduces the pressure losses, but a similar reduction can be achieved in the short-wavelength limit only if Pr is sufficiently large. The conditions marking the transition between a reduction to an enhancement of pressure losses, together with the size of the pressure losses themselves, are illustrated in figure 4 – to gauge the effectiveness of heating the reader is reminded that when $B = 2Re$ the pressure loss is zero. A plot of the mean buoyancy force as displayed in figure 5(*a*), which corresponds to the conditions used in figure 4(*a*), shows that this buoyancy force behaves in a similar fashion to the variations in the pressure-gradient correction. The shear at the right wall (see figure 5*b*) appears to be significantly reduced while that at the left wall generally increases, except when α and Pr are large. The reduction in the total shear force as displayed in figure 5(*d*) correlates well with both the formation of the mean buoyancy force and the reduction in the pressure gradient. An increase in Pr tends to strengthen the convection which in turn leads to an increase in the mean buoyancy force. When Pr is very large, the buoyancy effects are confined to a boundary layer adjacent to the heated wall and reduces the mean buoyancy force as a smaller portion of the flow field is exposed to temperature variations. The buoyancy force also seems to decrease in the long-wavelength limit $\alpha \to 0$ as the magnitude of the temperature gradient decreases. A reduction in the buoyancy force is also noted in the short-wavelength structure $\alpha \to \infty$; now the temperature gradient becomes concentrated within a thin boundary layer adjacent to the heated wall. Changes in the viscous forces occur owing to modifications to the flow pattern and this leads to a pressure-gradient reduction similar in size to that which can be attributed to the buoyancy force.

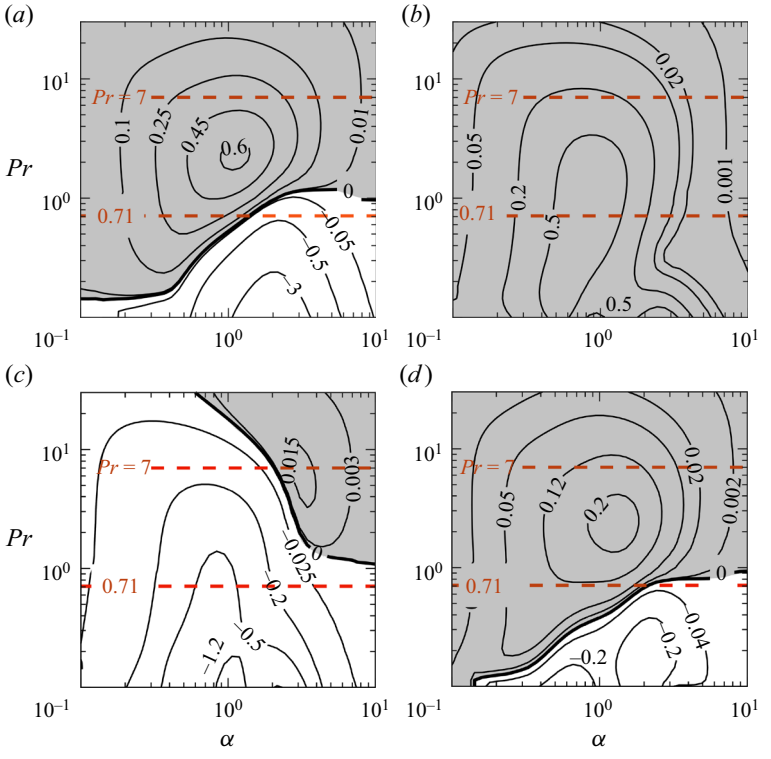

Figure 5. The form of (*a*) the buoyancy force F_b, (*b*) the force difference $\Delta F_R = F_R - F_{R,S}$, (*c*) the force difference $\Delta F_L = F_L - F_{L,S}$ and (*d*) the sum $\Delta F_R + \Delta F_L$ as functions of α and Pr. The Rayleigh number $Ra_{p,R} = 300$ and the Reynolds number $Re = 1$. The region of parameter space shaded grey identifies those conditions that correspond to a reduction in the losses.

To probe more deeply the properties of the flow structure we focused on the two values of the Prandtl number, $Pr = 0.71$ and 7; these were chosen as they are the values appropriate to air and water, respectively. The form of $B(\alpha)$ is illustrated in figure 6. It is evident that the largest absolute value of B occurs at some $\alpha = O(1)$ value and falls off towards zero as $\alpha \to 0$ and $\alpha \to \infty$ – these limits are analysed in the appendices. It is also noted that the sign of B changes at some $\alpha = O(1)$ whose value(s) is a function of the other parameters in the problem. For example, when $Pr = 0.71$ there appear to be two ranges of α; for relatively small values there is a reduction in the pressure losses but at larger values there is a significant increase of these losses. It seems that the critical value at which the transition between these contrasting behaviours occurs between these zones moves towards smaller α values as $Ra_{p,R}$ increases, see figure 6(*a*,*c*). The details of this response are only slightly affected by an increase in the Reynolds number from $Re = 1$ to $Re = 10$. The situation changes somewhat at the higher Prandtl number $Pr = 7$. Now a reduction in the pressure losses is observed for all values α unless $Ra_{p,R}$ becomes particularly large – this is illustrated in figure 5(*b*) for $Ra_{p,R} = 1000$ for which, over a small range of α, increasing losses are noted. An increase in Re from $Re = 1$ to $Re = 10$ sees the elimination of the short range. In summary we conclude that an increase in $Ra_{p,R}$ does not inevitably lead to a larger reduction in the pressure losses, and an increase in Re does not necessarily result in a modification of the pressure losses.

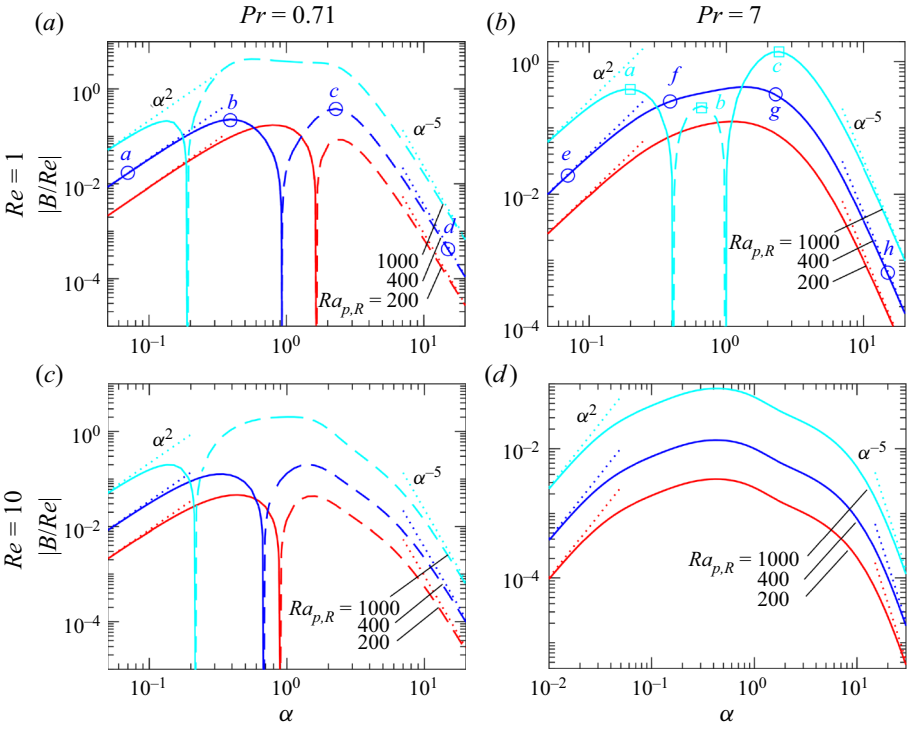

Figure 6. The variation in the pressure-gradient correction quantity $|B/Re|$ as a function of the heating wavenumber α. Dashed lines denote parameter combinations for which B/Re is negative.

The forms of the various forces that contribute to the flow dynamics when $Pr = 0.71$ and $Re = 1$ (appropriate to figure 6*a*) are depicted in figure 7(*a*); additional information that shows the changes in these forces relative to the base case of an isothermal channel is provided in figure 7(*b*). The right-wall shear force tends to moderate the pressure losses but the left-wall shear force increases the flow losses; which effect is the stronger depends on the particular flow parameters. The buoyancy force tends to reduce the losses at smallish values of α but appears to have the opposite effect at relatively large values of α. Taken overall, the combination of all these forces seems to reduce losses at small wavenumbers but increases them at shorter wavelengths. These remarks are naturally somewhat qualitative in nature as the detailed behaviour of the system response can change markedly with variation in Pr.

3.2. *The effect of the heating wavenumber α*

Figure 8 provides information that helps describe how the flow pattern adapts as the heating wavenumber changes. Long-wavelength heating generates large separation bubbles (figure 8*a*) whose size diminishes with increasing α (figure 8*b*,*c*) until they are confined to a thin boundary layer attached to the heated wall (figure 8*d*). If Pr is increased, the separation bubbles seem to shrink (see figure 8*e*–*h*).

The distributions of the shear forces corresponding to the conditions used in figure 8(*a*–*d*) are profiled in figure 9(*a*); the equivalent results pertaining to the higher Prandtl number $Pr = 7$ are shown in figure 9(*b*). These forces oscillate about a mean value whose size can change significantly according to the underlying flow conditions.

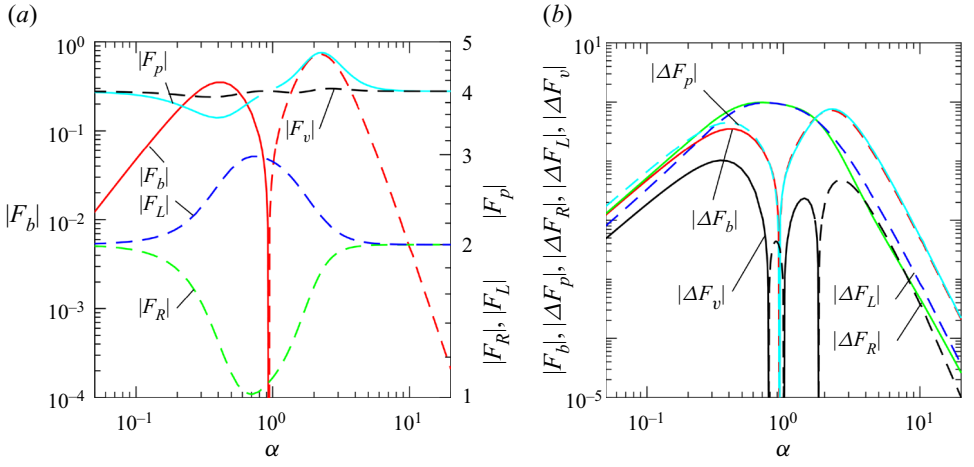

Figure 7. (*a*) The buoyancy force $|F_b|$, the viscous forces at the right $|F_R|$ and left $|F_L|$ walls and the pressure force $|F_p|$. All quantities plotted as functions of the heating wavenumber α. (*b*) Illustrates the variations of the viscous forces at the right $|\Delta F_R| = |F_R - F_{R,S}|$ and left $|\Delta F_L| = |F_L - F_{L,S}|$ walls, at both walls $|\Delta F_v| = |F_v - F_{v,S}|$ and the pressure force $|F_b|$. In all cases: $Ra_{p,R} = 400$, $Re = 1$, $Pr = 0.71$. Dashed lines denote negative values.

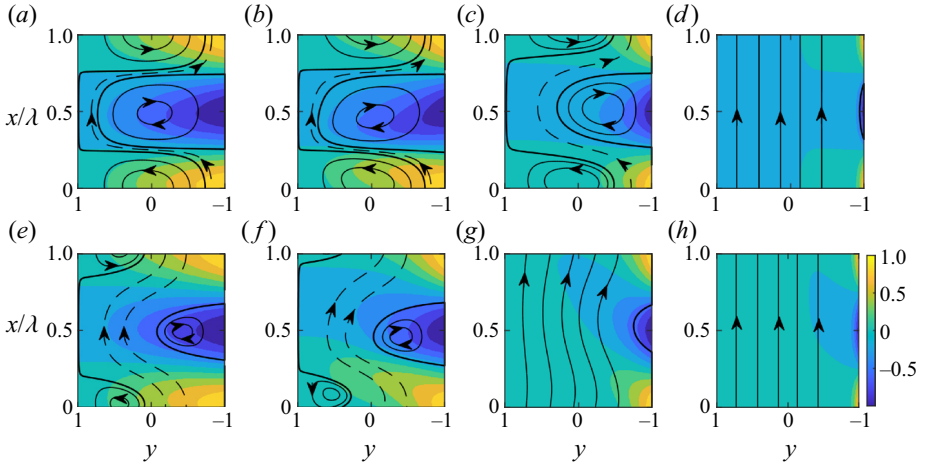

Figure 8. The flow and temperature fields for $Ra_{p,R} = 400$, $Re = 1$ and various values of α. Temperatures have been normalized by θ_{max}. In the top row the Prandtl number $Pr = 0.71$ while the wavenumber values are (*a*) $\alpha = 0.07$, (*b*) 0.39, (*c*) 2.29 and (*d*) 15. In the bottom row $Pr = 7$ with the same values α.

The shear forces tend to oppose the fluid movement in regions where the stream is in direct contact with the walls but tends to promote movement in those areas adjacent to separation bubbles. As the wavenumber increases so the extent of the separation bubbles and the amplitude of the shear variations both reduce. At larger values of Pr the amplitude of the shear variation is suppressed (cf. figure 9*a*,*b*).

3.3. *Variation in the heating intensity*

The data summarized in figure 10 provides a basis for the assessment of the effects of the heating intensity. The results suggest that at relatively modest values of Pr, e.g. $Pr = 0.71$,

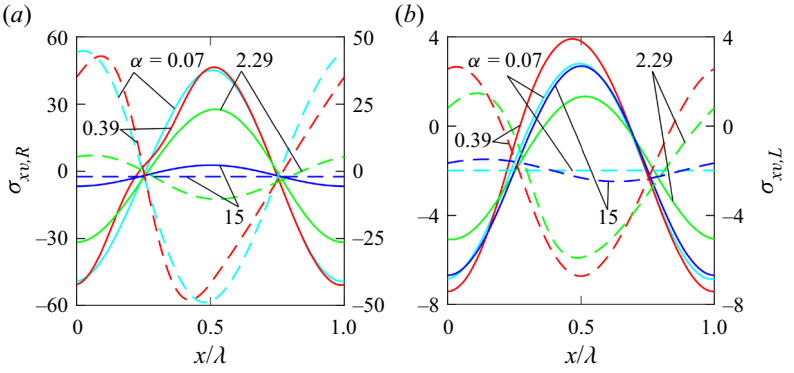

Figure 9. The distributions of the viscous forces at the right ($\sigma_{xv,R}$, solid lines) and the left ($\sigma_{xv,L}$, dashed lines) walls when $Ra_{p,R} = 400$, $Re = 1$ In (*a*) $Pr = 0.71$ while in (*b*) $Pr = 7$ and results are shown for the four wavenumbers used in figure 8 so $\alpha = 0.07,\ 0.39,\ 2.29$ and 15.

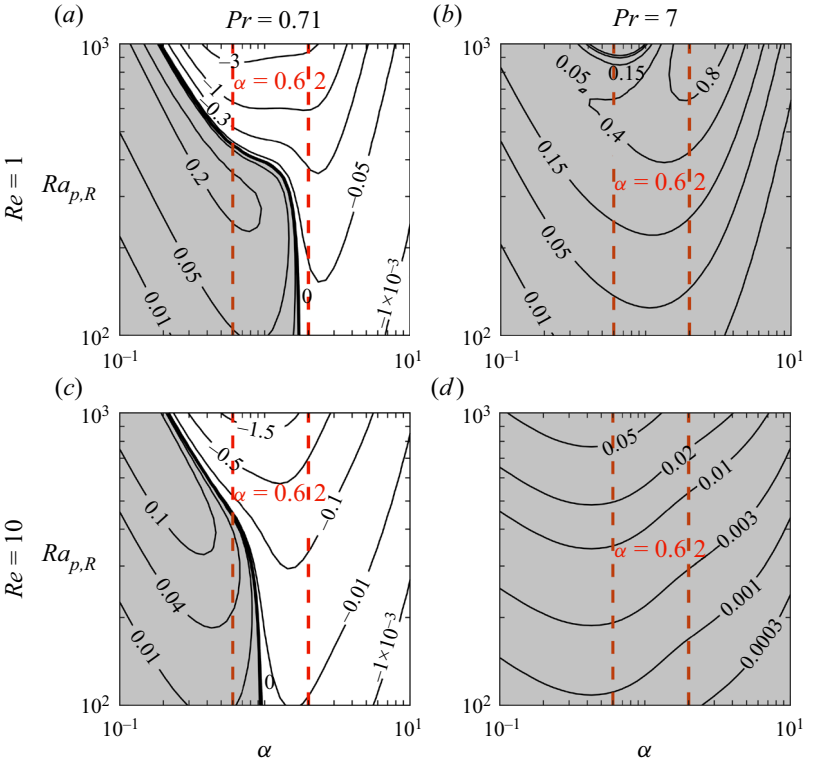

Figure 10. The variation in the pressure-gradient correction B/Re as a function of wavenumber α and Rayleigh number $Ra_{p,R}$. Grey shading identifies parameter combinations that lead to a reduction in the pressure losses.

an increase in $Ra_{p,R}$ at $\alpha <\sim 2$ initially reduces pressure losses, but this effect is transitory and substantial increases in $Ra_{p,R}$ ameliorate this effect; eventually, we get an increase in pressure losses for all values of Re used in this study (see figure 10*a*,*c*). Pressure losses appear to always increase with $Ra_{p,R}$ when a sufficiently large α is used. When $Pr = 7$ the reduction in losses increases with $Ra_{p,R}$ (figure 10*b*,*d*).

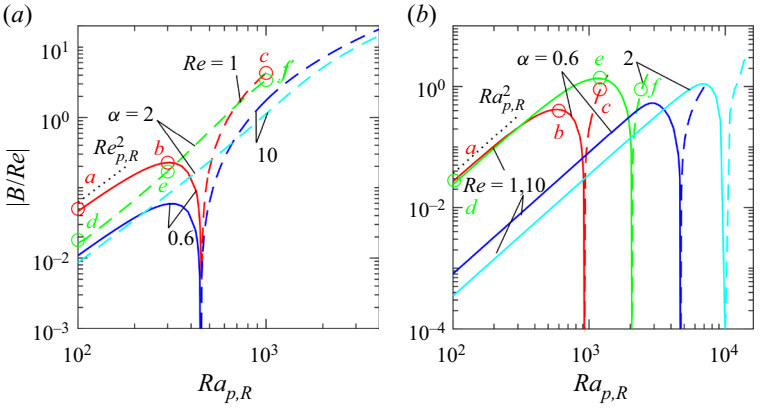

Figure 11. Variation in the pressure-gradient correction $|B/Re|$ as a function of $Ra_{p,R}$ when (*a*) $Pr = 0.71$ and (*b*) $Pr = 7$. Dashed lines denote parameter combinations for which B/Re is negative. The circular symbols correspond to the plots of the flow and temperature fields presented in figures 12 and 13.

Next, we explore the nature of the pressure losses as a function of $Ra_{p,R}$ for prescribed values of the wavenumber α. The forms of B are illustrated in figure 11 for two values of α; in figure 11(*a*) we have $\alpha = 0.6$, which lies solidly in the $B > 0$ region of figure 10(*a*), and in figure 11(*b*) we have $\alpha = 2$, for which $B < 0$. When $Pr = 0.71$ and $\alpha = 0.6$, B increases with $Ra_{p,R}$ until $Ra_{p,R} \approx 300$, then it starts to drop and becomes negative when $Ra_{p,R} > 450$ (figure 11*a*). When $\alpha = 2$, B is always negative and its magnitude grows with $Ra_{p,R}$. An increase in Reynolds number to $Re = 10$ changes the system response only in a marginal way (figure 11*a*). When $Pr = 7$, an increase in $Ra_{p,R}$ initially enhances B but this trend reverses when $Ra_{p,R}$ is relatively large leading to an increase in the pressure losses (figure 11*b*). It is of interest to note that the magnitude of B is in general roughly proportional to $Ra^2_{p,R}$ over the range studied.

The development of the flow and temperature fields as we increase $Ra_{p,R}$ are shown in figure 12 when $Pr = 0.71$. In all cases the growth of $Ra_{p,R}$ gives rise to larger separation bubbles and more intense movement within them. In the case of smaller α, the filling in of the space between the walls with the bubbles (see figure 12*a–c*) reduces the pressure gradient and eventually leads to an increase of these losses. The losses continually increase with $Ra_{p,R}$ at larger wavenumbers (see figure 12*d–f*). A comparison of all the panels in figure 12 demonstrates that it is not easy to predict the overall effect; for instance, the large bubbles in figure 12(*a*) lead to a decrease of pressure losses while, in contrast, the relatively small bubbles in figure 12(*d*) increase these losses.

The evolution of the flow and temperature patterns when $Pr = 7$ are illustrated in figure 13. It is interesting to observe that pressure losses are reduced at smallish $Ra_{p,R}$ (see figure 13*a*,*d*), which suggests that the buoyancy force is largely responsible for this effect. The addition of separation bubbles seems to promote the reduction of pressure losses (figure 13*b*,*e*); an effect that can ascribed to mitigation of the friction but, if these bubbles grow too large, the trend reverses and pressure losses grow (see figure 13*c*,*f*).

3.4. *The effect of the Reynolds number Re*

The effects of varying the size of the Reynolds number Re are addressed by the results summarized in figure 14. When Re is small and $Pr = 0.71$, heating at small α reduces the pressure losses while at larger wavenumbers these losses irrespective of the heating

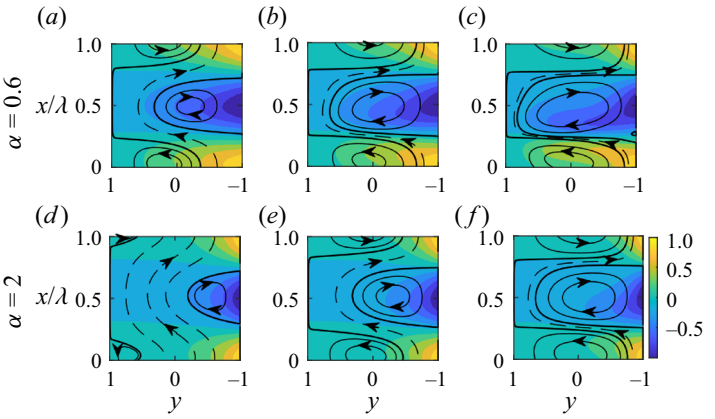

Figure 12. The flow and the temperature fields when $Re = 1$, $Pr = 0.71$. The three heating intensities correspond to $Ra_{p,R} = 100, 300$ and 1000; in (*a–c*) the wavenumber $\alpha = 0.6$ and in (*d–f*) $\alpha = 2$. The flow conditions used in these plots are marked by circles in figure 11(*a*).

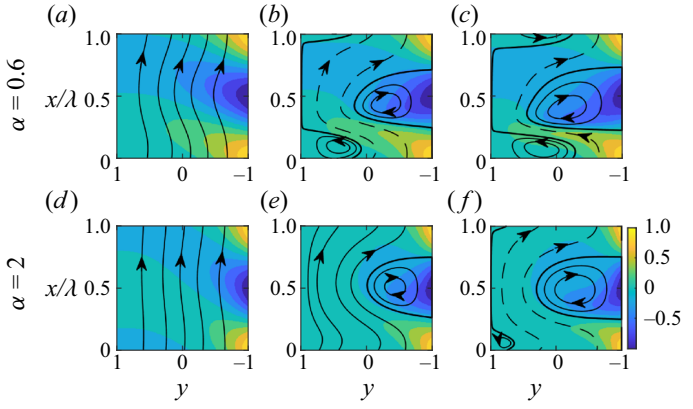

Figure 13. The flow and the temperature fields when $Re = 1$, $Pr = 7$. The three heating intensities correspond to $Ra_{p,R} = 100$, 600 and 1200 in (*a–c*) for which the wavenumber $\alpha = 0.6$; and to $Ra_{p,R} = 100$, 1200 and 2400 in (*d–f*) where $\alpha = 2$. The flow conditions used in these plots are marked by circles in figure 11(*b*).

intensity (figure 14*a*,*b*). An increase in Re appears to have minimal effect on the flow properties until Re approaches 1; after this, the magnitude of B starts to fall and this is accompanied by a concomitant decrease in the range of α over which B remains positive at lower values of $Ra_{p,R}$ (figure 14*a*). An increase in $Ra_{p,R}$ expands this interval at higher values of Re (figure 14*b*). When $Pr = 7$ the pressure losses are reduced for all wavenumbers, at least for the relatively weak heating rate $Ra_{p,R} = 400$, With an increase to $Ra_{p,R} = 800$ a window in the (α, Re)-plane is created at small values of Re in which losses increase (figure 14*d*). It is worth noting that this window closes as Re grows.

Some details of changes induced by varying Re are illustrated in figure 15 for the particular wavenumbers $\alpha = 0.6$ and $\alpha = 2$. There appears to be a well-defined asymptote as $Re \to 0$ in all cases but the value of B can be of either sign depending on the parameter values. An increase in Re at the lower heating rate of $Ra_{p,R} = 400$ initially mitigates the loss reduction and but there is an eventual increase in this loss when $\alpha = 0.6$. A similar effect is observed at the larger heating rate $Ra_{p,R} = 800$. The situation is somewhat similar for $Pr = 7$; now there are well-defined positive asymptotes as $Re \to 0$ in all cases except

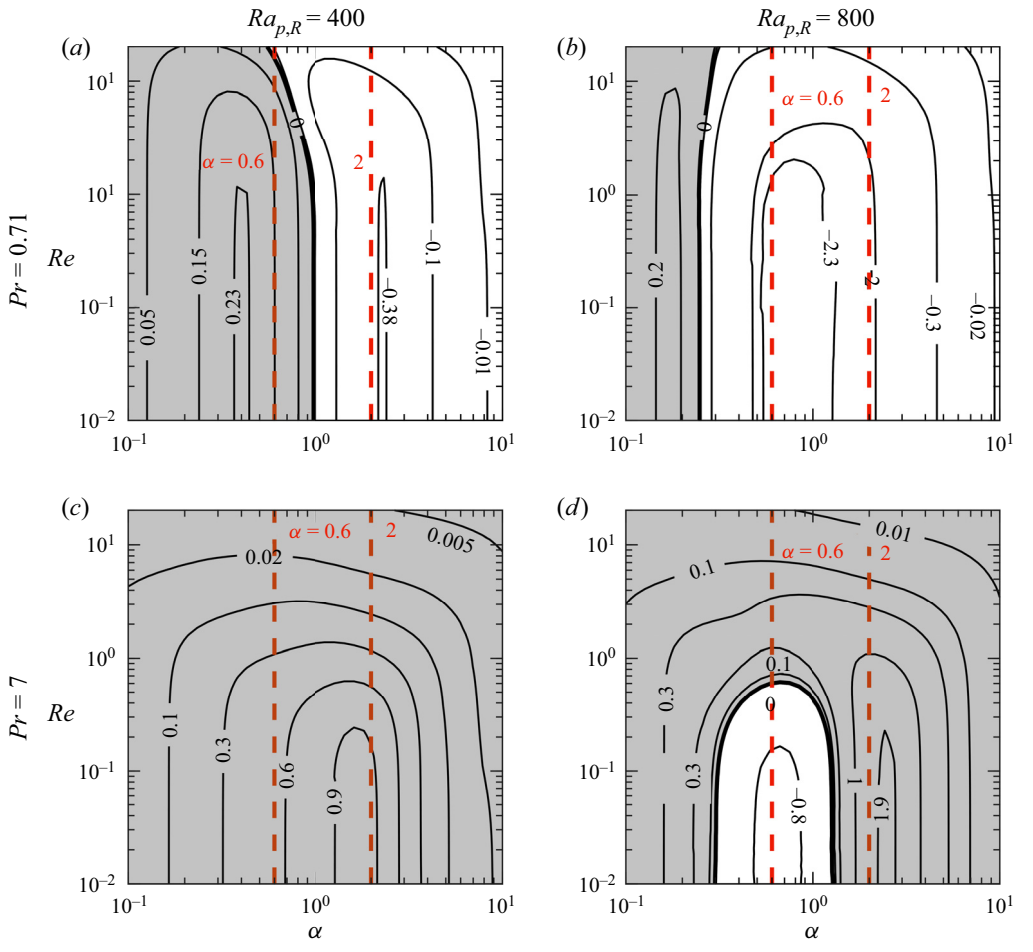

Figure 14. The variation of the pressure-gradient correction B/Re as a function of α and Re and for the parameter combinations $(Pr,\ Ra_{p,R}) = (a)\ (0.71, 400)$, $(b)\ (0.71,800)$, $(c)\ (7,400)$ and $(d)\ (7,800)$. Grey shading indicates parameter combinations that lead to a reduction in the pressure losses.

when $(\alpha, Ra_{p,R}) = (0.6, 800)$ for which B is negative (figure 15*b*). An increase in Re leads to a reduction of B, except for this special case for which an increase in Re first leads to an increase of B, which becomes positive, reaches a maximum when $Re \approx 3$ and then begins to decrease roughly proportional to Re^{-2} (figure 15*b*).

The evolution of the flow patterns for various values Re has already been discussed for $Pr = 0.71$ (see figure 2). With a greater Prandtl number $Pr = 7$ there is a much quicker elimination of the separation bubbles, with the flow becoming virtually rectilinear by the stage $Re = 20$ (see figure 16) (cf. we previously noted that this only happens once $Re = 100$ when $Pr = 0.71$). This can be explained in terms of the temperature field becoming almost uniform at smaller Re for larger Pr; at this stage, convective effects dominate their conductive counterparts.

We close our description of these one-wall heating problems by noting that all the flows considered have fluid directed upwards (against gravity). This is not unduly restrictive for it is straightforward to generalize our finding to downward problems. This can be accomplished by nothing that if we change the sign of the buoyancy term in the

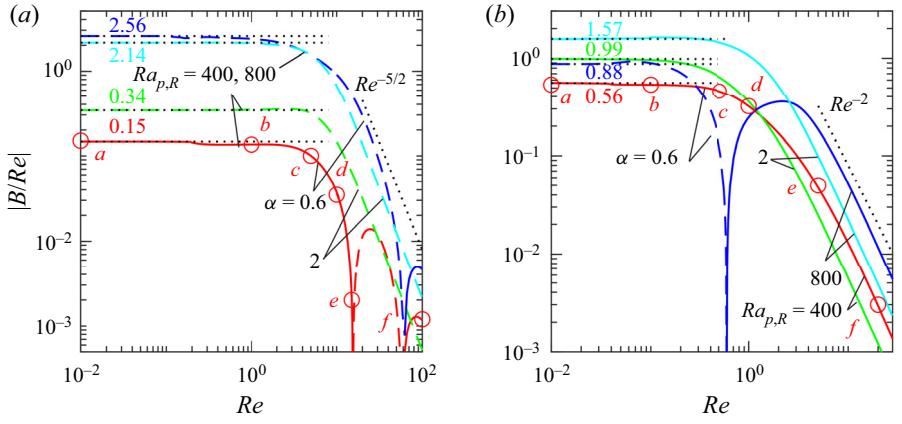

Figure 15. The variation of the pressure-gradient correction $|B/Re|$ as a function of Re when (*a*) $Pr = 0.71$, (*b*) $Pr = 7$. Dashed lines denote negative values. The flow and temperature patterns for condition marked with circles in figure 15(*a*) are displayed in figure 2 and those marked by circles in figure 15(*b*) are displayed in figure 16.

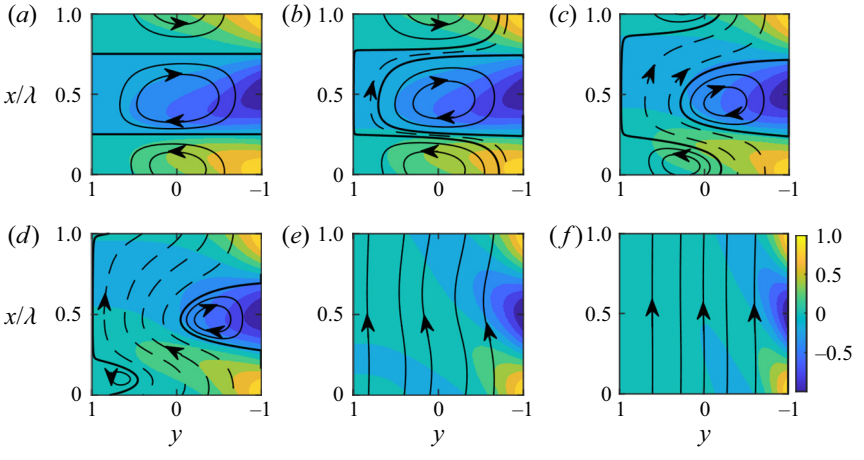

Figure 16. The flow and temperature fields corresponding to the parameter values $Ra_{p,R} = 400$, $Pr = 7$, $\alpha = 0.6$. Panels show increasing values of Re; (*a*) $Re = 0$, (*b*) 0.1, (*c*) 0.5, (*d*) 1, (*e*) 5 and (*f*) 20. The temperature has been normalized using θ_{max}. The flow conditions used in these figures are marked with circles in figure 15(*b*).

x-momentum equation (2.3*a*) – the flow is directed towards the positive x-axis and the gravity vector is directed towards the positive x-axis. An inspection of (2.3) then shows that the solution remains unchanged under the transformations $\theta \to -\theta$, $x \to x + \lambda/2$. In other words, we conclude that the results for downward flows can be inferred directly from the calculations described above and the need for further separate computations is therefore rendered unnecessary. We are grateful to a referee for pointing out that these symmetries can only hold if the transport fluid properties are constant and will necessarily be broken in more realistic non-isothermal circumstances.

4. Heating applied to both walls

We now turn our attention to examining the problem when both walls of the slot are heated. It is perhaps unsurprising that in this configuration the relative position of the two heating patterns is a crucial factor that affects the performance of the system. We remind the

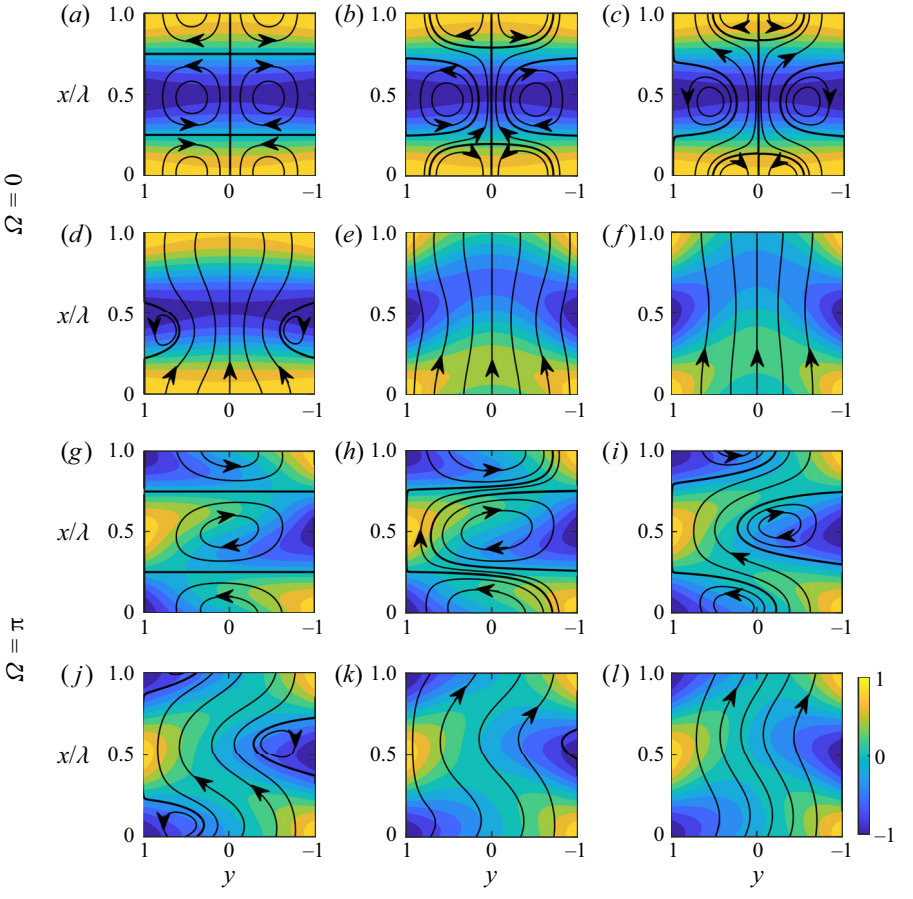

Figure 17. The flow and temperature fields when the two walls are heated equally strongly with $Ra_{p,R} = Ra_{p,L} = 200$. The wavenumber $\alpha = 0.6$. In (*a–f*) the hot spots are aligned so $\Omega = 0$; the Reynolds number $Re =$ (*a*) 0, (*b*) 0.1, (*c*) 0.2, (*d*) 1, (*e*) 10 and (*f*) 20. In (*g–l*) the hot spots on one wall are opposite the cold spots on the other so $\Omega = \pi$. In the calculations $Re =$ (*g*) 0, (*h*) 1, (*i*) 5, (*j*) 10, (*k*) 15 and (*l*) 20. The temperature has been normalized with θ_{max}.

reader that it is the phase difference Ω (see definition (2.2)) that is used to prescribe the relative patterning; $\Omega = 0$ corresponds to hot spots at the walls being aligned in the horizontal direction while $\Omega = \pi$ corresponds to hot spots at one wall opposite cold spots on the other. We shall restrict our discussion mainly to $Pr = 0.71$ because this enables us to describe the plethora of possible system responses without being overwhelmed by numerous parameter combinations.

The flow and temperature fields when the hot spots are aligned exhibit a left/right symmetry, as shown in figure 17(*a–f*). Pure natural convection leads to the formation of two columns of counter-rotating rolls, as shown in figure 17(*a*). Heating-induced modulations of small Re flows lead to the trapping of fluid in the middle of the channel at positions next to the hot spots as well as the formation of separation bubbles at the height of the cold spots (see figure 17*b*). The net upwards flow takes the form of a stream tube which flows between the separation bubbles and then divides into two smaller stream tubes which surround the in-flow stagnation zones (figure 17*b*,*c*). An increase in Re reduces the extent of the in-flow stagnation zones as well as the separation bubbles and then washes away

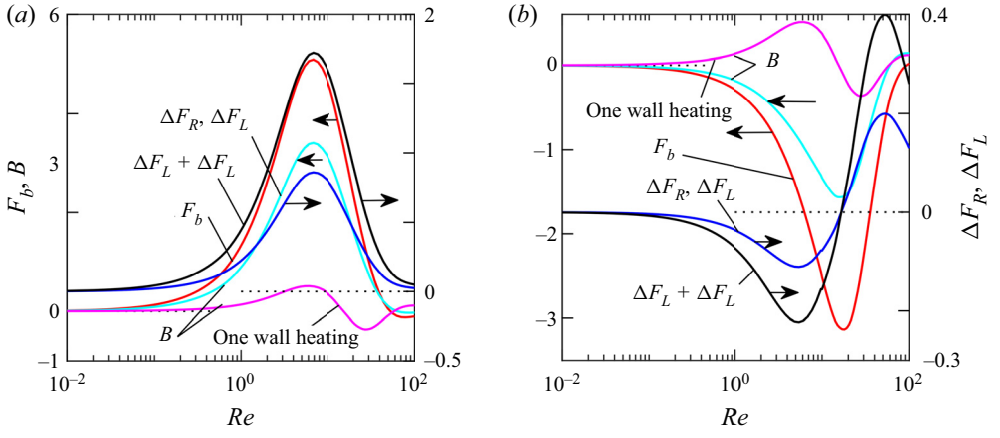

Figure 18. The mean buoyancy force F_b, the viscous force differences at the right and left walls $\Delta F_R = F_R - F_{R,S}$, $\Delta F_L = F_L - F_{L,S}$, the sum $\Delta F_R + \Delta F_L$ and the pressure-gradient correction B. These quantities are shown as functions of Re with $Ra_{p,R} = Ra_{p,L} = 200$, $Pr = 0.71$, $\alpha = 0.6$. The pressure-gradient correction for the one-wall heating case with $Ra_{p,R} = 400$ has been superimposed for reference. (*a*) $\Omega = 0$ and (*b*) $\Omega = \pi$.

the stagnation zones (figure 17*d*) before eliminating the separation bubbles (figure 17*e*). Eventually, the remnant flow becomes rectilinear (figure 17*f*). In figure 17(*g–l*) we show the contrasting problem $\Omega = \pi$ for which the flow and temperature fields do not possess any obvious symmetries. Now pure natural convection takes the form of a single column of counter-rotating rolls. Heating-induced modulations of the small-Re flows lead to creation of separation bubbles attached to the cold spots (figure 17*h–k*). The net upwards flow takes the form of a single stream tube which meanders between the bubbles. As Re increases the bubbles shrink and eventually are washed away (figure 17*l*).

Modifications of the flow and temperature fields lead to forces whose structure strongly depend on Ω. When $\Omega = 0$, the two-wall heating leads to a reduction in pressure losses by up to an order of magnitude compared with the one-wall heating results. The range of Re over which such a reduction is possible is depicted in figure 18 and both the amelioration of shear forces and the increase in the net buoyancy force contribute to this effect. The situation is qualitatively different when $\Omega = \pi$ as then the two-wall heating increases the pressure losses across a wide range of Re. We contrast this with the one-wall heating results for which losses can be reduced at certain values of Re (see figure 18*b*); the reason for this can be ascribed to the net buoyancy force.

The evolution of the flow and temperature fields as functions of the wavenumber are illustrated in figure 19 when $\Omega = 0$. The structure starts as a nearly rectilinear flow in the small-α limit; as the wavenumber increases separation bubbles form on both sides of the channel; eventually, their growth ceases and they are eliminated when α is sufficiently large. The situation is somewhat different when $\Omega = \pi$ as then the separation bubbles are in existence even at small values α and these slowly shrink as α grows before the flow becomes effectively rectilinear.

It is helpful to comment briefly on the changes associated with an increase in Pr as this leads to strengthening of the convective effects. The evolution of the flow and temperature fields for the same conditions as in figure 19 but now with $Pr = 7$ are illustrated in figure 20. When there is no heating offset $\Omega = 0$ there is no evidence of any separation bubbles irrespective of the wavenumber. On the other hand, separation bubbles are formed

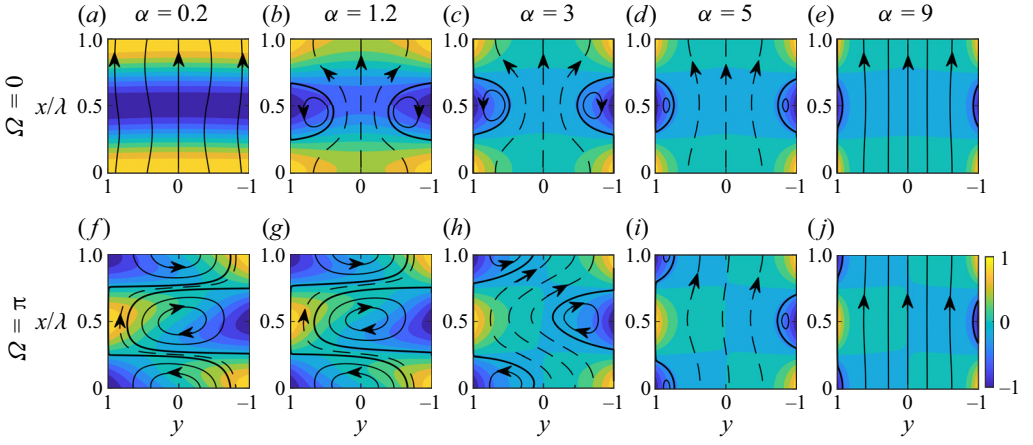

Figure 19. The flow and the temperature fields when $Ra_{p,R} = Ra_{p,L} = 200$, $Re = 1$, $Pr = 0.71$. The temperature has been normalized with θ_{max}. Results are shown at the five wavenumbers $\alpha = 0.2$, 1.2, 3, 5 and 9; in the top row the phase offset $\Omega = 0$ and in the lower row $\Omega = \pi$.

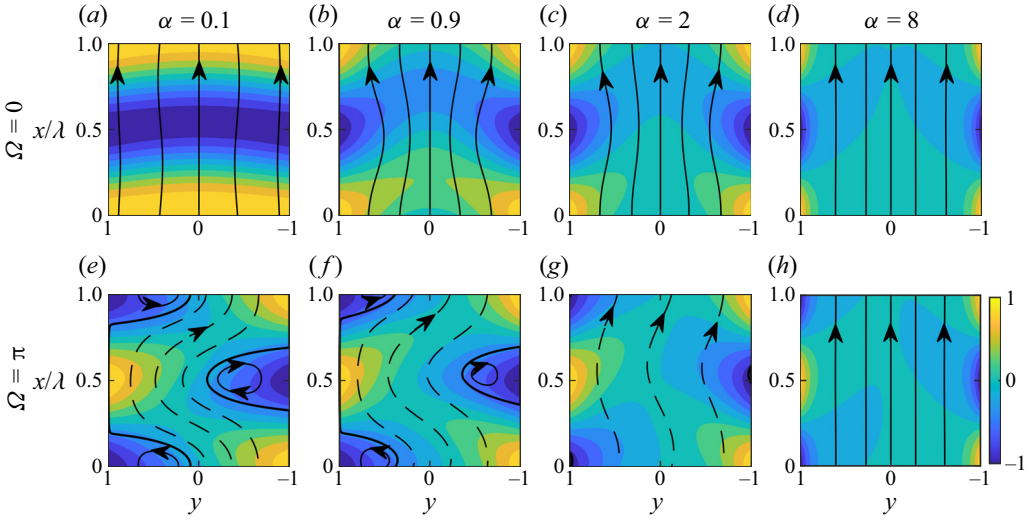

Figure 20. The flow and the temperature fields when $Ra_{p,R} = Ra_{p,L} = 200$, $Re = 1$, $Pr = 7$. The temperature has been normalized with θ_{max}. Results are shown at the four wavenumbers $\alpha = 0.1$, 0.9, 2 and 8; in the top row the phase offset $\Omega = 0$ and in the lower row $\Omega = \pi$.

when $\Omega = \pi$ but now they are much weaker than their counterparts observed in figure 19 when $Pr = 0.71$.

Detailed information concerning the pressure-gradient reduction is provided in figure 21. These data pertain to the problem with the same heating intensity at the two walls with $Ra_{p,R} = Ra_{p,L} = 200$. For comparison purposes, these plots also include data relevant to the single-wall heating with a doubled heating intensity so that $Ra_{p,R} = 400$, $Ra_{p,L} = 0$. An inspection of the two data sets provides a simple means by which one may estimate any possible gain associated either with the one-wall heating or by some heating to each wall. When $Pr = 0.71$, two-wall heating with $\Omega = 0$ leads to a pressure-gradient reduction perhaps an order of magnitude larger than the one-wall

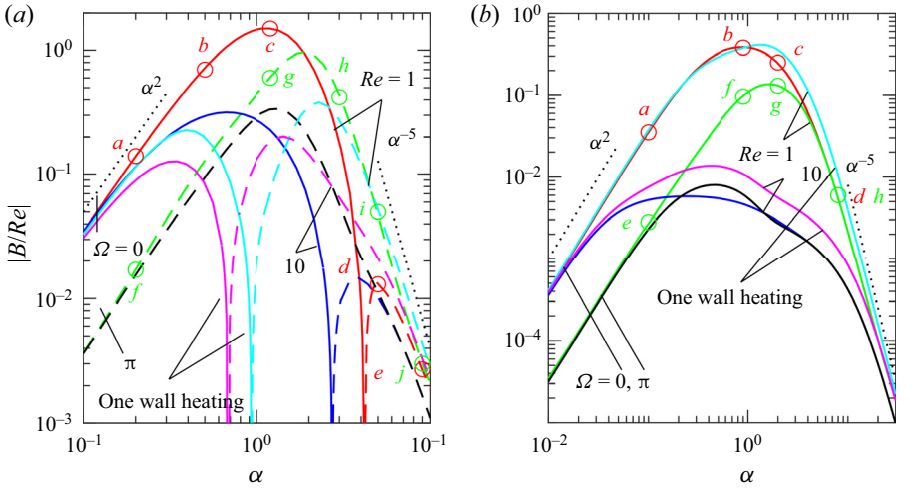

Figure 21. The pressure-gradient correction $|B/Re|$ as a function of α when $Ra_{p,R} = Ra_{p,L} = 200$, $\Omega = 0$ and $\Omega = \pi$. The results for the one-wall heating $Ra_{p,R} = 400$, $Ra_{p,L} = 0$ have been included for reference. Dashed lines represent negative values. (*a*) $Pr = 0.71$ and (*b*) $Pr = 7$.

heating results. Moreover, it extends the range of wavenumbers over which such a reduction is possible (figure 21*a*). The use of two-wall heating with $\Omega = \pi$ is detrimental as it appears to increase the pressure loss over the whole α range (figure 21*a*). When the fluid is water, for which $Pr = 7$, two-wall heating with $\Omega = 0$ produces effects similar to those resulting from one-wall heating but the use of $\Omega = \pi$ produces results that are actually worse than their one-wall counterparts (figure 21*b*). We remark that the heating has minimal influence on the pressure gradient in both the small- and large-α limits regardless of the values of Ω and Pr. The maximum effect on the pressure gradient occurs when $\alpha \approx 1 - 2$; it also seems that $B \propto \alpha^2$ as $\alpha \to 0$ and $B \propto \alpha^{-5}$ as $\alpha \to \infty$ and these predictions are confirmed by some asymptotic analysis described in the appendices.

Our discussion so far has been restricted to the extremes in the relative positioning of the heating patterns. Variations in the pressure losses regarded as a function of Ω is displayed in figure 22 confirm that, indeed, the data determined for $\Omega = 0$ and $\Omega = \pi$ represent the extremes in the possible values of B. The optimal system performance is achieved when $\Omega = 0$ and an unfortunate selection of Ω can be enough to switch reductions in pressure losses to increases at a sufficiently small Pr.

The role played by Pr is illustrated in figure 23 for the extreme configurations $\Omega = 0$ and $\Omega = \pi$. The results clearly demonstrate the attractiveness of employing $\Omega = 0$; indeed, using $\Omega = \pi$ gives outcomes less good than those that provided by single-wall heating. The drawbacks of using $\Omega = \pi$ include a reduction in the achievable pressure losses, a restriction on the heating wavenumbers that correspond to a pressure reduction and a smaller range of Pr over which pressure reductions are feasible.

The final question to be addressed here relates to a characterization of the system response when the walls are exposed to different heating intensities. The results shown in figure 24 correspond to the situation when one of the walls is heated twice as strongly as the other. These findings can be compared with the data pertaining to equal heating configuration summarized in figure 22. The weakening of the heating of one wall moderates the magnitude of loss reduction but the qualitative dependence on the other parameters remains largely unchanged.

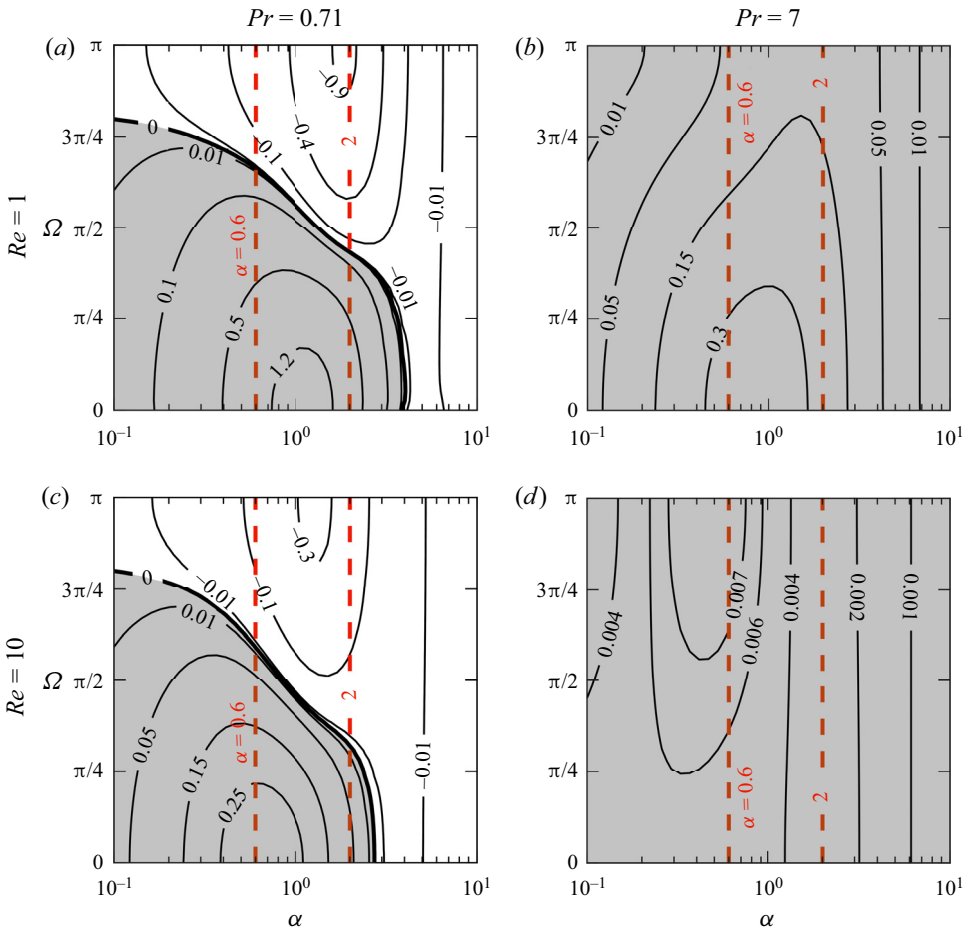

Figure 22. The pressure-gradient correction B/Re as a function of α and Ω when $Ra_{p,R} = Ra_{p,L} = 200$. Here, we have two Reynolds numbers $Re = 1$ (*a*,*b*) and 10 (*c*,*d*) and two values of Pr: 0.71 (*a*,*c*) and 7 (*b*,*d*). Grey shading identifies conditions that lead to a reduction in the pressure losses.

5. Discussion

The reduction of pressure losses in conduits is of interest as a mechanism for controlling the cost of energy associated with fluid transportation. Our analysis has explored the potential of using patterned heating for restricting pressure losses in laminar flows through vertical channels. Using patterned heating in this way is particularly attractive as it sidesteps the need for large temperature differences. Here, we have supposed that the heating distribution takes a sinusoidal form characterized by the wavenumber α and with an amplitude specified in terms of an appropriate Rayleigh number. This heating can be applied to one wall or both; in this latter instance this brings into play the consideration of the phase offset between the two patterns. We have assumed that the fluid is Boussinesq, and the field equations have been solved numerically to spectral accuracy. We have managed to develop explicit analytic solutions in the large and small α limits and we have demonstrated that these show excellent agreement with the computations. We posed the problem as one in which we asked the size of the pressure-gradient correction required to preserve the flow rate in the heated channel compared with the reference isothermal case.

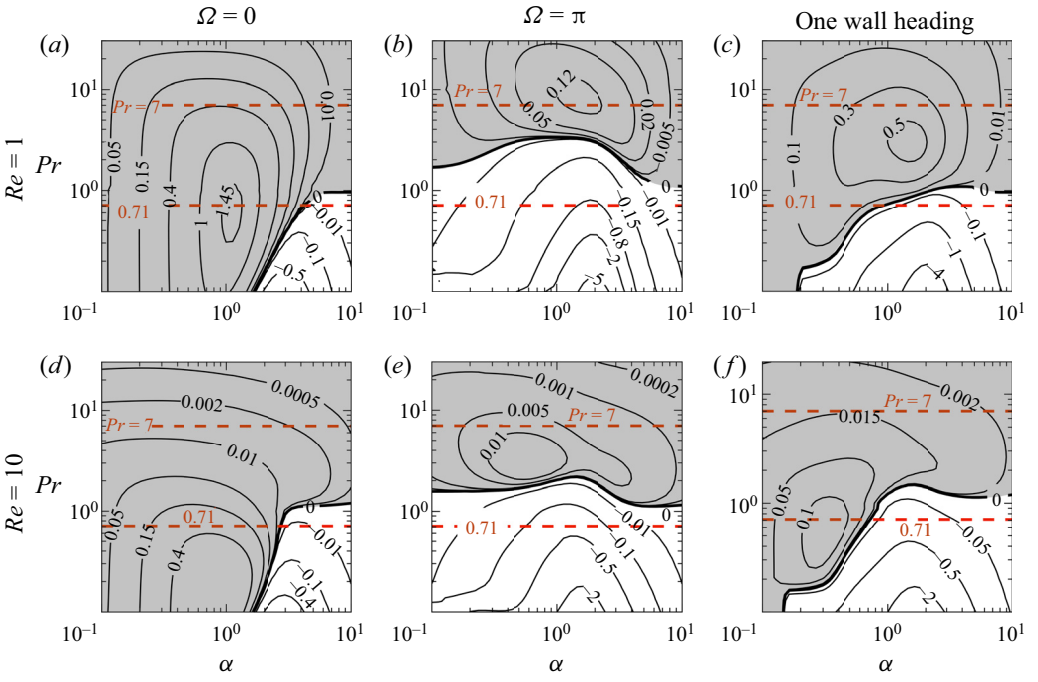

Figure 23. The pressure-gradient correction B/Re as a function of α and Pr for two-wall heating with $Ra_{p,R} = Ra_{p,L} = 200$ and the one-wall heating with $Ra_{p,R} = 400$. The grey shading identifies those conditions that lead to a reduction in the pressure losses.

We have seen that the heating generates separation bubbles which play a central role in minimizing the pressure losses. These bubbles reduce the direct contact between the stream and the sidewalls, thereby reducing frictional resistance. Furthermore, the bubbles restructure the temperature field, and this leads to the formation of a net buoyancy force which counterbalances the pressure losses. The appearance of these bubbles reduces the effective flow area, which tends to promote pressure losses. Owing to the multiplicity of the effects that feed into the system dynamics, its response can exhibit a wide range of characteristics as the various parameters change. An accurate prediction of the response with a particular combination of parameter values necessitates detailed analysis and it is difficult to draw useful conclusions that hold over a wide range of cases. With sufficient increase in the flow Reynolds number, the separation bubbles are washed away, and this eliminates the pressure-gradient-reducing effect completely. Our calculations suggest that heating is most effective when $\alpha = 0(1)$ and is of somewhat limited use in the small and large wavenumber limits. The system response appears to be sensitive to variations in the Prandtl number; this can be explained by noting that, as Pr grows, the convective effects intensify, and these are responsible for the modification of the temperature field and hence the net buoyancy force. The heating of both walls can lead to a pattern interaction effect and an adjustment in the relative position of the two distributions can change the system response by as much as an order of magnitude. We have demonstrated that the optimal effect is achieved when the hot spots on the two walls are aligned horizontally.

One question that has not been addressed in this study concerns the stability of our solution structures. It is well known that thermally stratified shear channel flows such as Rayleigh–Bénard flows or pressure-driven laminar flows in differentially heated channels

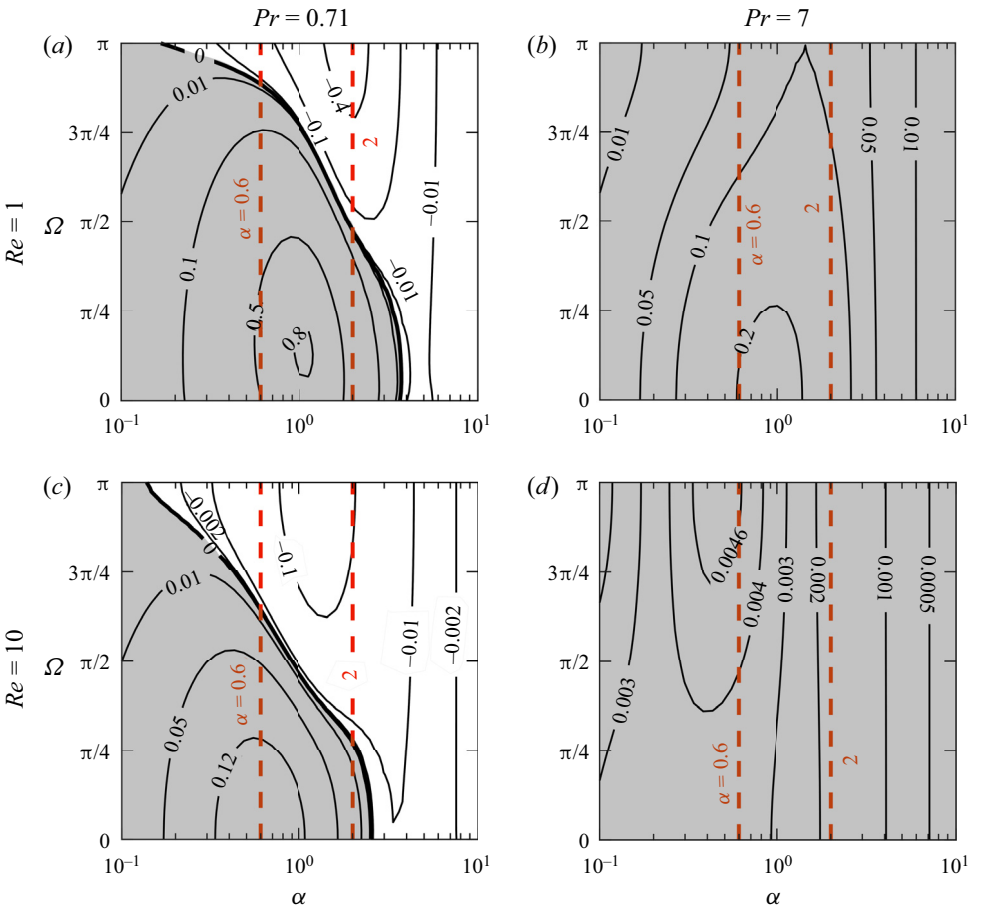

Figure 24. The pressure-gradient correction B/Re as a function of α and Ω when $Ra_{p,R} = 200$, $Ra_{p,L} = 100$. Regions shaded grey identify conditions that leads to a reduction in the pressure losses.

tend to be three-dimensional and unsteady. These very classical results pertain to uniform wall heating while our study has been focussed on patterned heating with the mean temperatures of the walls being equal. There seems to be very few studies into the stability of patterned convection, although Hossain & Floryan (2015*b*) have looked at this issue in a horizontal channel. It is very likely that there is a threshold beyond which the flow passes through a stability limit after which the flow becomes three-dimensional. Clearly, the next step in a study of the present problem would be a careful stability analysis of the flow to ascertain the point beyond which the system will no longer exhibit pressure losses when subjected to patterned heating.

In summary, we have shown that a significant and dramatic reduction in the pressure losses can be achieved if the various flow parameters are chosen carefully. As far as we know, these results are novel and potentially significant. They provide some general guidelines as to how the various problem parameters may be chosen and how the heating patterns may be arranged to achieve optimal results. The quantitative details of the system properties are naturally functions of the heating distribution, its strength, the flow Reynolds number and the Prandtl number. Carefully chosen heating of the two walls can induce a pattern interaction effect and a judicious choice can have as much as an order of

magnitude effect on the system response. It would be of interest to know whether more intricate heating distributions might improve our scope in further reducing the pressure losses. There is also the issue as to how our ideas might generalize to other geometries. In this regard, our present calculations have been restricted to vertical conduits and we are currently looking at how the various conclusions are modified should the slot be inclined. We claim that, whilst many properties of patterned heating may be relatively well understood, in this paper we have established the unexpected result that it can give rise to a rather large reduction in pressure losses. In turn, this implies a potentially considerable saving in the energy expended in maintaining the flow. Whilst many practically important and relevant fluid flows are far more complicated than our idealized motion through a heated vertical conduit of the type envisioned here, we have shown that patterned heating may play a significant role in controlling important properties of physically and practically important flow configurations.

Acknowledgements. We are indebted to the three referees whose numerous comments and suggestions have led to a dramatic improvement in the manuscript.

Funding. This work has been carried out with support from NSERC of Canada.

Declaration of interests. The authors report no conflict of interests.

Author ORCIDs.
J.M. Floryan https://orcid.org/0000-0003-3296-4122;
W. Wang https://orcid.org/0000-0001-8547-2047;
Andrew P. Bassom https://orcid.org/0000-0003-3275-7801.

Appendix A. Long-wavelength heating

In this appendix we look at the properties of the patterned convection in the long-wavelength limit $\alpha \ll 1$. We do this by introducing the stretched coordinate $X = \alpha x$ which brings the governing equations and thermal boundary conditions to the following form:

$$\alpha[Re(1-y^2)+u_1]u_{1X} + v_1(-2Re\, y + u_{1y}) = -\alpha p_{1X} + \alpha^2 u_{1XX} + u_{1yy} + \frac{1}{Pr}\theta_1, \quad \text{(A1}a\text{)}$$

$$\alpha[Re(1-y^2)+u_1]v_{1X} + v_1 v_{1y} = -p_{1y} + \alpha^2 v_{1XX} + v_{1yy}, \quad \text{(A1}b\text{)}$$

$$\alpha[Re(1-y^2)+u_1]\theta_{1X} + v_1\theta_{1y} = \frac{1}{Pr}(\alpha^2\theta_{1XX} + \theta_{1yy}), \quad \text{(A1}c\text{)}$$

$$\alpha u_{1X} + v_{1y} = 0, \quad \text{(A1}d\text{)}$$

with the thermal boundary conditions becoming

$$\theta_1(X,-1) = \tfrac{1}{2}Ra_{p,R}\cos X \quad \text{and} \quad \theta_1(X,1) = \tfrac{1}{2}Ra_{p,L}\cos(X+\Omega). \quad \text{(A2}a,b\text{)}$$

It is helpful for the subsequent calculations to define three related quantities

$$R_1 = Ra_{p,R} + Ra_{p,L}\cos\Omega, \quad R_2 = Ra_{p,R} - Ra_{p,L}\cos\Omega \quad \text{and} \quad R_3 = Ra_{p,L}\sin\Omega. \quad \text{(A3}a\text{–}c\text{)}$$

When $\alpha \ll 1$ we seek solutions which assume the structure

$$(u_1, v_1, p_1, \theta_1) = \alpha^{-1}(0,0,\hat{P}_{-1},0) + (\hat{U}_0, 0, \hat{P}_0, \hat{\theta}_0) + \alpha(\hat{U}_1, \hat{V}_0, \hat{P}_1, \hat{\theta}_1) + \alpha^2(\hat{U}_2, \hat{V}_1, \hat{P}_2, \hat{\theta}_2) + \cdots, \quad \text{(A4)}$$

where all the unknowns are functions of X and y. Given the form of the boundary conditions we are led to the zeroth-order solutions

$$\hat{U}_0 = -\frac{1}{24\,Pr}y(1-y^2)(R_2\cos X + R_3\sin X), \quad \hat{V}_0 = -\frac{1}{96\,Pr}(1-y^2)^2(R_3\cos X - R_2\sin X), \tag{A5a,b}$$

$$\hat{\theta}_0 = \tfrac{1}{4}[(R_1 - R_2 y)\cos X - R_3(1+y)\sin X] \quad \text{and} \quad \hat{P}_{-1} = \frac{1}{4\,Pr}(R_1\sin X + R_3\cos X). \tag{A5c,d}$$

The $O(\alpha)$ thermal field consists of both mean and X-dependent parts. It may be shown that

$$\hat{\theta}_1(X,y) = -\tfrac{1}{4}Pr\,Re[F_1(y)\sin X + F_2(y)\cos X] + \tfrac{1}{384}[F_3(y)\sin 2X + F_4(y)\cos 2X + F_5(y)], \tag{A6}$$

where the polynomials $F_1(y) - F_5(y)$ are defined to be

$$F_1(y) = \tfrac{1}{60}(1-y^2)[5(y^2-5)R_1 - y(3y^2-7)R_2], \tag{A7a}$$

$$F_2(y) = \tfrac{1}{60}R_3(1-y^2)(3y^3+5y^2-7y-25), \tag{A7b}$$

$$F_3(y) = \tfrac{1}{60}(1-y^2)(3y^4-2y^2-17)(R_3^2-R_2^2) - \tfrac{1}{30}y(1-y^2)(7-3y^2)(R_3^2+R_1R_2), \tag{A7c}$$

$$F_4(y) = \tfrac{1}{30}(1-y^2)(3y^4+3y^3-2y^2-7y-17)R_2R_3 - \tfrac{1}{30}y(1-y^2)(3y^2-7)R_1R_3, \tag{A7d}$$

$$F_5(y) = -\tfrac{1}{30}y(1-y^2)(7-3y^2)(R_1+R_2)R_3. \tag{A7e}$$

It then follows that

$$\hat{U}_1(X,y) = \frac{ReR_3}{10\,080}\left(F_6 - \frac{F_7}{Pr}\right)\cos X + \frac{Re}{10\,080}\left(F_8 + R_2\frac{F_7}{Pr}\right)\sin X + \hat{U}_{M1}(y), \tag{A8a}$$

$$\hat{V}_1(X,y) = \frac{ReR_3}{10\,080}\left(F_9 - \frac{F_{10}}{Pr}\right)\sin X + \frac{Re}{10\,080}\left(F_{11} - R_2\frac{F_{10}}{Pr}\right)\cos X, \tag{A8b}$$

and

$$\hat{P}_0 = \tfrac{17}{210}Re(R_3\sin X - R_1\cos X), \tag{A8c}$$

in which the polynomials $F_6(y) - F_{11}(y)$ are given by

$$F_6(y) = (1-y^2)(3y^5+7y^4-18y^3-98y^2+31y+19), \tag{A9a}$$

$$F_7(y) = y(y^2-1)(5y^4-16y^2+19), \tag{A9b}$$

$$F_8(y) = (y^2-1)[(3y^5-18y^3+31y)R_2 - (7y^4-98y^2+19)R_1], \tag{A9c}$$

$$F_9(y) = -\tfrac{1}{8}(y^2-1)^2(3y^4+8y^3-22y^2-152y+51), \tag{A9d}$$

$$F_{10}(y) = \tfrac{1}{8}(y^2-1)^2(5y^4-18y^2+29), \tag{A9e}$$

and

$$F_{11}(y) = -\tfrac{1}{8}(y^2-1)^2[(3y^4-22y^2+51)R_2 - 8y(y^2-19)R_1]. \tag{A9f}$$

Furthermore, the mean part of the streamwise velocity $\hat{U}_{M1}(y)$ is another polynomial but this consists only of terms of odd degree so the mass flux across the slot $-1 \le y \le 1$

is zero. The full forms of $\hat{U}_1$, $\hat{V}_1$ and $\hat{P}_0$ also incorporate higher harmonics in X but these do not play a part in what follows so are not recorded.

We now move onto consideration of the $O(\alpha^2)$ terms. If we suppose that the pressure gradient

$$p_X = A\,\alpha^2 + \cdots, \tag{A10}$$

then the $O(\alpha^2)$ terms in the streamwise momentum and energy equations are

$$\begin{aligned} &Re(1-y^2)\hat{U}_{1X} - 2Re\,y\,\hat{V}_1 + \hat{U}_0\hat{U}_{1X} + \hat{U}_1\hat{U}_{0X} + \hat{V}_0\hat{U}_{1y} + \hat{V}_1\hat{U}_{0y} \\ &\qquad = -(A + \cdots) + \hat{U}_{0XX} + \hat{U}_{2yy} + \frac{1}{Pr}\hat{\theta}_2, \end{aligned} \tag{A11a}$$

$$Re(1-y^2)\hat{\theta}_{1X} + \hat{U}_0\hat{\theta}_{1X} + \hat{U}_1\hat{\theta}_{0X} + \hat{V}_0\hat{\theta}_{1y} + \hat{V}_1\hat{\theta}_{0y} = \frac{1}{Pr}(\hat{\theta}_{0XX} + \hat{\theta}_{2yy}). \tag{A11b}$$

If we denote the mean part of $\hat{\theta}_2(x, y)$ by $\hat{\theta}_{2M}(y)$ then the mean parts of (A11*b*) furnish an expression for $(\hat{\theta}_{2M})_{yy}$ that can be integrated twice subject to the requirement that $\hat{\theta}_{2M}$ vanishes at $y = \pm 1$. This result is substituted into (A11*a*) for the mean function $\hat{U}_{2M}(y)$ which can be found subject to $\hat{U}_{2M}(\pm 1) = 0$; the pressure gradient is then adjusted to ensure that the mean mass flux is zero. After considerable algebraic manipulation we find that

$$A = \frac{Re}{227026800\,Pr^2}\left\{\begin{array}{l}(Ra_{p,L}^2 + Ra_{p,R}^2 - 2Ra_{p,L}\,Ra_{p,R}\cos\Omega)(51 - 790\,Pr) \\ \quad +[5876(Ra_{p,L}^2 + Ra_{p,R}^2) + 9620\,Ra_{p,L}Ra_{p,R}\cos\Omega]Pr^2\end{array}\right\}, \tag{A12}$$

and the pressure gradient is then $B = A\,\alpha^2$. When heating is applied at the right wall only, the above expression simplifies to the form

$$B = \alpha^2\frac{ReRa_{p,R}^2}{227026800\,Pr^2}(51 - 790\,Pr + 5876\,Pr^2), \tag{A13}$$

a quantity which is positive for any Pr which means that such heating always reduces pressure losses. The same conclusion holds for heating applied at the left wall only.

To determine the mean Nusselt number, we take the expression for $\hat{\theta}_{2M}$ and evaluate the derivative at $y = -1$ to find that

$$\left.\frac{\mathrm{d}\hat{\theta}_{2M}}{\mathrm{d}y}\right|_{y=-1} = \frac{1}{45\,360}Re(Ra_{p,R}^2 - Ra_{p,L}^2)(1 - 10\,Pr), \tag{A14}$$

which leads to

$$Nu_{av} = -\alpha^2\lambda^{-1}\int_{x_0}^{x_0+\lambda}\left.\frac{\mathrm{d}\hat{\theta}_{2M}}{\mathrm{d}y}\right|_{y=-1}\mathrm{d}x = -\frac{\alpha^3}{45\,360}Re(Ra_{p,R}^2 - Ra_{p,L}^2)(1 - 10\,Pr). \tag{A15}$$

To assess the veracity of our results, we display in figure 25 a comparison of the asymptotic predictions against some numerical simulations of the full governing system. We plot the form of B as given by (A13) and the Nusselt number Nu_{av} predicted by (A15). The comparison shows excellent agreement between the analytical and numerical findings, at least for wavenumbers $\alpha < 0.1$.

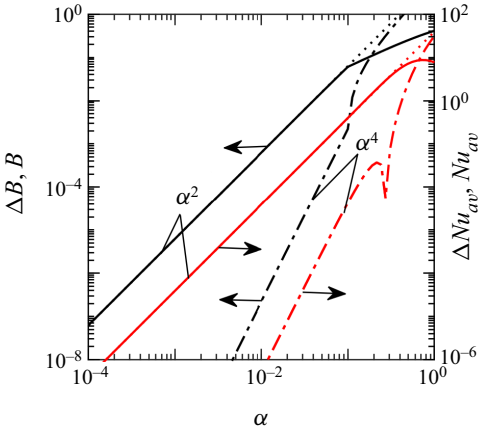

Figure 25. Comparisons of the numerically and analytically determined pressure-gradient correction B and the average Nusselt number Nu_{av} for long-wavelength heating with $Re = 3$, $Ra_{p,R} = 312$, $Ra_{p,L} = 0$, $Pr = 0.71$. Dotted lines identify analytical solutions B_a and $Nu_{av,a}$ as given by (A13) and (A15), respectively, while the solid lines identify the corresponding numerical solutions B_n and $Nu_{av,n}$. The dashed-dotted lines identify the differences $\Delta B = |B_a - B_n|$ and $\Delta Nu = |Nu_{av,n} - Nu_{av,a}|$ which appear to be of size $O(\alpha^4)$. Black lines relate to the pressure-gradient parameter B while red lines correspond to Nu_{av}.

Appendix B. Short-wavelength heating

When α is large most of the interesting motion takes place near the walls; given this we again put $X = \alpha x$ and introduce $Y = \alpha(y + 1)$ near the right-hand wall. Written in terms of these the governing equations become

$$\alpha\left[Re\left(\frac{2Y}{\alpha} - \frac{Y^2}{\alpha^2}\right) + u_1\right]u_{1X} + v_1\left[2Re\left(1 - \frac{Y}{\alpha}\right) + \alpha u_{1Y}\right] = -\alpha p_{1X} + \alpha^2(u_{1XX} + u_{1YY}) + \frac{\theta_1}{Pr}, \tag{B1a}$$

$$\alpha\left[Re\left(\frac{2Y}{\alpha} - \frac{Y^2}{\alpha^2}\right) + u_1\right]v_{1X} + \alpha v_1 v_{1Y} = -\alpha p_{1Y} + \alpha^2(v_{1XX} + v_{1YY}), \tag{B1b}$$

$$u_{1X} + v_{1Y} = 0, \tag{B1c}$$

$$\alpha\left[Re\left(\frac{2Y}{\alpha} - \frac{Y^2}{\alpha^2}\right) + u_1\right]\theta_{1X} + \alpha v_1\theta_{1Y} = \frac{\alpha^2}{Pr}(\theta_{1XX} + \theta_{1YY}). \tag{B1d}$$

We solve these equations subject to the periodic heating on the edges of the slot so that

$$\theta_1(X, -1) = \tfrac{1}{2}\,Ra_{p,R}\cos X, \quad \theta_1(X, 1) = \tfrac{1}{2}Ra_{p,L}\cos(X + \Omega). \tag{B2a,b}$$

When $\alpha \gg 1$ we seek solutions which assume the structure

$$u_1 = \alpha^{-2}\left(\sum_0^\infty \alpha^{-j}\hat{U}_j\right), \quad v_1 = \alpha^{-2}\left(\sum_0^\infty \alpha^{-j}\hat{V}_j\right),$$
$$p_1 = \alpha^{-1}\left(\sum_0^\infty \alpha^{-j}\hat{P}_j\right), \quad \theta_1 = \left(\sum_0^\infty \alpha^{-j}\hat{\Theta}_j\right), \tag{B3a–d}$$

where all the unknowns are functions of X and Y. Leading-order terms in the thermal equation simply give

$$\hat{\Theta}_{0XX} + \hat{\Theta}_{0YY} = 0 \Rightarrow \hat{\Theta}_0(X, Y) = \tfrac{1}{2} Ra_{p,R} \exp(-Y) \cos X, \tag{B4}$$

in order to satisfy the boundary condition on $Y = 0$ and to decay as $Y \to \infty$. The next-order equations simply show that $\hat{\Theta}_1(X, Y) \equiv 0$; we also have $\hat{U}_1 = \hat{V}_1 = \hat{P}_1 \equiv 0$. At $O(\alpha^{-2})$ we find that

$$2YRe\, \hat{\Theta}_{0X} = \frac{1}{Pr}(\hat{\Theta}_{2XX} + \hat{\Theta}_{2YY}) \Rightarrow \hat{\Theta}_2(X, Y) = \frac{1}{4} Pr\, Re\, Ra_{p,R} Y(Y + 1) \exp(-Y) \sin X, \tag{B5}$$

while $O(1)$ terms in the two momentum and the continuity equations give

$$0 = -\hat{P}_{0X} + \hat{U}_{0XX} + \hat{U}_{0YY} + \frac{1}{Pr}\hat{\Theta}_0, \quad 0 = -\hat{P}_{0Y} + \hat{V}_{0XX} + \hat{V}_{0YY}, \quad \hat{U}_{0X} + \hat{V}_{0Y} = 0, \tag{B6a–c}$$

whose solution is

$$\hat{U}_0 = \frac{Ra_{p,R}}{16\, Pr} Y(2 - Y) \exp(-Y) \cos X, \quad \hat{V}_0 = \frac{Ra_{p,R}}{16\, Pr} Y^2 \exp(-Y) \sin X, \quad \hat{P}_0 = \frac{Ra_{p,R}}{8\, Pr}(1 + 2Y) \exp(-Y) \sin X. \tag{B7a–c}$$

We next return to the energy equation at $O(\alpha^{-3})$. We have that

$$\hat{U}_0 \hat{\Theta}_{0X} + \hat{V}_0\, \hat{\Theta}_{0Y} - Re\, Y^2 \hat{\Theta}_{0X} = \frac{1}{Pr}(\hat{\Theta}_{3XX} + \hat{\Theta}_{3YY}), \tag{B8}$$

which, on substituting the leading-order results, becomes

$$\hat{\Theta}_{3XX} + \hat{\Theta}_{3YY} = -\tfrac{1}{32} Ra_{p,R}^2\, Y \exp(-2Y) \sin 2X + \tfrac{1}{2} Pr\, Re\, Ra_{p,R} Y^2 \exp(-Y) \sin X, \tag{B9}$$

which admits the solution

$$\hat{\Theta}_3(X, Y) = -\tfrac{1}{24}(2Y^2 + 3Y + 3) Y \exp(-Y) Pr\, Re\, Ra_{p,R} \sin X + \tfrac{1}{512} Ra_{p,R}^2\, Y(1 + 2Y) \exp(-2Y) \sin 2X. \tag{B10}$$

We also need to solve the problem for $\hat{U}_2$, $\hat{V}_2$ and $\hat{P}_2$. Given the forms of the leading-order solutions (B4) and (B7) the relevant equations can be written

$$\hat{U}_{2XX} + \hat{U}_{2YY} - \hat{P}_{2X} = \frac{Ra_{p,R}\, Re}{8\, Pr} Y \exp(-Y)[Y(Y - 1) - 2\, Pr(Y + 1)] \sin X, \tag{B11}$$

$$\hat{V}_{2XX} + \hat{V}_{2YY} - \hat{P}_{2Y} = \frac{Ra_{p,R}\, Re}{8\, Pr} Y^3 \exp(-Y) \cos X, \quad \hat{U}_{2X} + \hat{V}_{2Y} = 0. \tag{B12a,b}$$

The solution of this system is

$$\hat{U}_2 = \frac{Re\, Ra_{p,L}}{8\, Pr}\left[-\frac{1}{12} Y(Y^3 - Y^2 - 3Y - 12) + \frac{Pr}{24}(-Y^4 + 2Y^3 + 9Y^2 - 6Y)\right] \times \exp(-Y) \sin X, \tag{B13a}$$

$$\hat{V}_2 = \frac{Re\, Ra_{p,L}}{8\, Pr}\left[-\frac{Y^2}{12}(Y^2 + 3Y + 6) + \frac{Pr}{24} Y^2(3 - 2Y - Y^2)\right] \exp(-Y) \cos X, \tag{B13b}$$

and

$$\hat{P}_2 = \frac{Re\, Ra_{p,L}}{8\, Pr}\left[\frac{1}{6}(2Y^3-3Y^2+3Y+9) - \frac{Pr}{12}(4Y^3+12Y^2+12Y+15)\right]\exp(-Y)\cos X. \tag{B13c}$$

It may be checked that at $O(\alpha^{-3})$ and $O(\alpha^{-4})$ in the streamwise momentum equation the nonlinear terms cannot generate any mean terms so, fortunately, we do not need to deal with them in any detail. At $O(\alpha^{-4})$ in the energy equation we have

$$2Y\, Re\, \hat{\Theta}_{2X} = \frac{1}{Pr}(\hat{\Theta}_{4XX} + \hat{\Theta}_{4YY}) \Rightarrow \hat{\Theta}_4(X, Y) \propto \exp(-Y)\cos X. \tag{B14}$$

We move to the fifth-order problem and find that

$$\frac{1}{Pr}(\hat{\Theta}_{5XX} + \hat{\Theta}_{5YY}) = 2Y\, Re\, \hat{\Theta}_{3X} - ReY^2\hat{\Theta}_{2X} + \hat{U}_0\hat{\Theta}_{2X} + \hat{U}_2\hat{\Theta}_{0X} + \hat{V}_0\hat{\Theta}_{2Y} + \hat{V}_2\hat{\Theta}_{0Y}. \tag{B15}$$

Now, in view of the leading-order solutions, together with the second-order results, the nonlinear terms here will generate mean terms. If this mean component is denoted as $\hat{\Theta}_{5M}(Y)$ then

$$\frac{\mathrm{d}^2\hat{\Theta}_{5M}}{\mathrm{d}Y^2} = \frac{Re\, Ra_{p,R}^2}{384} Y\exp(-2Y)[2Y^3+2Y^2+3Y-12+Pr(3+3Y+6Y^2-5Y^3)]. \tag{B16}$$

This can be integrated twice subject to $\hat{\Theta}_{5M}(0) = 0$ and the requirement that $\hat{\Theta}_{5M}$ remains bounded as $Y \to \infty$. Then we obtain

$$\hat{\Theta}_{5M} = \frac{Ra_{p,R}^2 Re}{1024}\left[(8\, Pr-9)\{(1-(1+2Y+2Y^2)\exp(-2Y)\} - \frac{2}{3}Y^3\exp(-2Y)\{\, Pr(5Y+14) - 2(Y+5)\}\right]. \tag{B17}$$

The streamwise momentum equation at $O(\alpha^{-5})$ gives

$$2Y\, Re\, \hat{U}_{3X} - Y^2\, Re\, \hat{U}_{2X} + \hat{U}_0\hat{U}_{2X} + \hat{U}_2\hat{U}_{0X} + 2\, Re\, \hat{V}_3 - 2Y\, Re\, \hat{V}_2 + \hat{V}_0\hat{U}_{2Y} + \hat{V}_2\hat{U}_{0Y} = -\hat{P}_{5X} + \hat{U}_{5XX} + \hat{U}_{5YY} + \frac{\hat{\Theta}_5}{Pr}. \tag{B18}$$

We are again interested in the mean parts of this equation. If we suppose that $\hat{P}_{5M} = AX$ then let us consider the mean part of $\hat{U}_5$, call it $\hat{U}_{5M}(Y)$. Fortunately, we do not need to solve for the full form of $\hat{U}_{5M}(Y)$; instead, it is sufficient to note that for large Y we have

$$\hat{U}_{5M} \sim \left[A - \frac{Ra_{p,R}^2\, Re}{128}\left(1 - \frac{9}{8\, Pr}\right)\right]\frac{1}{2}Y^2. \tag{B19}$$

This completes the analysis of the wall layer. We see that the $O(\alpha^{-5})$ component of θ_1 tends to a constant as $Y \to \infty$ (see (B17)) while the $O(\alpha^{-7})$ component of u_1 grows quadratically.

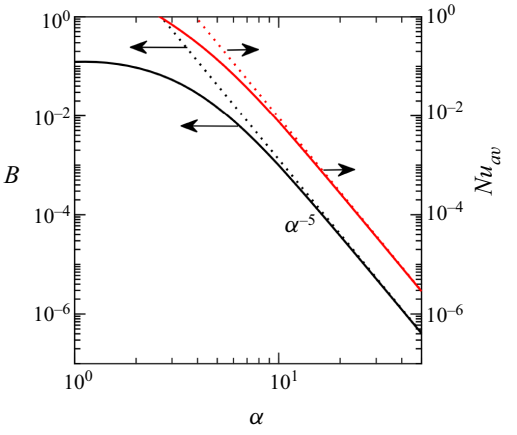

Figure 26. A comparison of the numerically and analytically determined pressure-gradient correction B and the average Nusselt number Nu_{av} for short-wavelength heating with $Re = 1$, $Ra_{p,R} = 200$, $Ra_{p,L} = 0$, $Pr = 7$. The dotted and solid lines identify the analytical and numerical solutions, respectively. The black lines relate to B while red refers to Nu_{av}.

Thus, across the bulk of the slot where $y = O(1)$ we have that

$$u_1 = \alpha^{-5}\tilde{U}(y) + \cdots, \quad \theta_1 = \alpha^{-5}\tilde{\Theta}(y) + \cdots, \quad p_1 = \alpha^{-5}Ax + \cdots, \tag{B20a–c}$$

and these satisfy

$$0 = -A + \frac{\mathrm{d}^2\tilde{U}}{\mathrm{d}y^2} + \frac{1}{Pr}\tilde{\Theta}, \quad \frac{\mathrm{d}^2\tilde{\Theta}}{\mathrm{d}y^2} = 0. \tag{B21a,b}$$

The form of (B17) shows that for matching we require

$$\tilde{\Theta} \to \frac{Ra_{p,R}^2 Re}{128}\left(Pr - \frac{9}{8}\right) \text{ as } y \to -1. \tag{B22}$$

An exactly parallel calculation at the left-hand wall shows that we must also demand that

$$\tilde{\Theta} \to -\frac{Ra_{p,L}^2 Re}{128}\left(Pr - \frac{9}{8}\right) \text{ as } y \to 1. \tag{B23}$$

Hence

$$\tilde{\Theta}(y) = \frac{Re}{256}\left(Pr - \frac{9}{8}\right)[Ra_{p,R}^2 - Ra_{p,L}^2 - (Ra_{p,L}^2 + Ra_{p,R}^2)y], \tag{B24}$$

so that

$$\frac{\mathrm{d}^2\tilde{U}}{\mathrm{d}y^2} = A - \frac{Re}{256\,Pr}\left(Pr - \frac{9}{8}\right)[Ra_{p,R}^2 - Ra_{p,L}^2 - (Ra_{p,L}^2 + Ra_{p,R}^2)y]. \tag{B25}$$

If we integrate twice and demand $\tilde{U}(\pm 1) = 0$ this determines that

$$A = \frac{Re}{256\,Pr}\left(Pr - \frac{9}{8}\right)(Ra_{p,R}^2 + Ra_{p,L}^2). \tag{B26}$$

In conclusion, we see that to maintain a constant mass flux through the channel we need to impose a pressure-gradient correction $B = \alpha^{-5}A$ where A is given by (B26). The sign

of the pressure-gradient correction depends on Pr with the reduction of pressure losses occurring only if $Pr > \frac{9}{8}$.

In figure 26 we compare our asymptotic predictions against some numerical simulations. We see excellent agreement between the two cases for $\alpha > 10$.

References

Abtahi, A. & Floryan, J.M. 2017*a* Natural convection in corrugated slots. *J. Fluid Mech.* **815**, 537–569.

Abtahi, A. & Floryan, J.M. 2017*b* Natural convection and thermal drift. *J. Fluid Mech.* **826**, 553–582.

Abtahi, A. & Floryan, J.M. 2018 On the formation of thermal drift. *Phys. Fluids* **30**, 043602.

Andreozzi, A., Buonomo, B. & Manca, O. 2005 Numerical study of natural convection in vertical channels with adiabatic extensions downstream. *Numer. Heat Transfer* A*: Applics.* **47**, 741–762.

Bénard, H. 1900 Les tourbillons cellulaires dans une nappe liquide. *Revue Gen. Sci. Pure Appl.* **11**, 1261–1271.

Floryan, J.M., Baayoun, A.W., Panday, S. & Bassom, A.P. 2022*a* Patterned convection in inclined slots. *J. Fluid Mech.* **950**, A11.

Floryan, D. & Floryan, J.M. 2015 Drag reduction in heated channels. *J. Fluid Mech.* **765**, 353–395.

Floryan, J.M., Haq, N. & Panday, S. 2022*b* Horizontal chimney effect. *Trans. ASME J. Heat Transfer* **144**, 072601.

Floryan, J.M. & Inasawa, A. 2021 Pattern interaction effect. *Sci. Rep.* **11**, 14573.

Floryan, J.M., Shadman, S. & Hossain, M.Z. 2018 Heating-induced drag reduction in relative movement of parallel plates. *Phys. Rev. Fluids* **3**, 094101.

Floryan, J.M., Wang, W., Panday, S. & Bassom, A.P. 2022*c* Natural convection and pattern interaction in a two-dimensional vertical slot. *J. Fluid Mech.* **946**, A20.

Frőhlich, J., Laure, P. & Peyret, R. 1992 Large departures from Boussinesq approximation in the Rayleigh-Bénard problem. *Phys. Fluids* A **4**, 1355–1372.

Gandossi, L. & Von Estorff, U. 2015 An overview of hydraulic fracturing and other formation stimulation technologies for shale gas production – Update 2015. *Scientific and Technical Research Report*. Joint Research Centre of the European Commission; Publications Office of the European Union.

Hossain, M.Z. & Floryan, J.M. 2013 Instabilities of natural convection in a periodically heated layer. *J. Fluid Mech.* **733**, 33–67.

Hossain, M.Z. & Floryan, J.M. 2014 Natural convection in a fluid layer periodically heated from above. *Phys. Rev.* E **90**, 023015.

Hossain, M.Z. & Floryan, J.M. 2015*a* Natural convection in a horizontal fluid layer periodically heated from above and below. *Phys. Rev.* E **92**, 023015.

Hossain, M.Z. & Floryan, J.M. 2015*b* Mixed convection in a periodically heated channel. *J. Fluid Mech.* **768**, 51–90.

Hossain, M.Z. & Floryan, J.M. 2016 Drag reduction in a thermally modulated channel. *J. Fluid Mech.* **791**, 122–153.

Hossain, M.Z. & Floryan, J.M. 2020 On the role of surface grooves in the reduction of pressure losses in heated channels. *Phys. Fluids* **32**, 083610.

Hossain, M.Z. & Floryan, J.M. 2022 Wavenumber lock-in and spatial parametric resonance in convection. *J. Fluid Mech.* **944**, A47.

Hossain, M.Z., Floryan, D. & Floryan, J.M. 2012 Drag reduction due to spatial thermal modulations. *J. Fluid Mech.* **713**, 398–419.

Hughes, G.O. & Griffiths, R.W. 2008 Horizontal convection. *Annu. Rev. Fluid Mech.* **40**, 185–208.

Inasawa, A., Hara, K. & Floryan, J.M. 2021 Experiments on thermal drift. *Phys. Fluids* **33**, 087116.

Inasawa, A., Taneda, K. & Floryan, J.M. 2019 Experiments on flows in channels with spatially distributed heating. *J. Fluid Mech.* **872**, 177–197.

Linden, P.F. 1999 The fluid mechanics and natural ventilation. *Annu. Rev. Fluid Mech.* **31**, 201–238.

Mehiris, A., Ameziani, D., Rahli, O., Bouhadef, K. & Bennacer, R. 2017 Active chimney effect using heated porous layers: optimum heat transfer. *Eur. Phys. J. Appl. Phys.* **78**, 34807.

Mohammadi, A. & Floryan, J.M. 2012 Mechanism of drag generation by surface corrugation. *Phys. Fluids* **24**, 013602.

Mortensen, D.K., Walker, I.S. & Sherman, M. 2011 Energy and air quality implications of passive stack ventilation in residential buildings. *Ernest Orlando Lawrence Berkeley National Laboratory Report* LBNL-4589E.

NAGLER, J. 2021 Numerical simulation of a mixed vertical ventilation system. *Z Angew. Math. Mech.* **101**, e201900353.

NAYLOR, D., FLORYAN, J.M. & TARASUK, J.D. 1991 A numerical study of developing free convection between isothermal vertical plates. *Trans. ASME J. Heat Transfer* **113**, 620–626.

NOVAK, M. & FLORYAN, J.M. 1995 Free convection in systems of vertical channels. *Intl J. Heat Fluid Flow* **16**, 244–253.

PAOLUCCI, S. 1982 On the filtering of sound from the Navier-Stokes equations. *Report No. SAND* 82-8257. Sandia National Laboratories.

PUTNAM, J.O. 1882 *The Open Fire for All Ages*. James R. Osgood and Company.

RAYLEIGH, LORD 1916 On convection currents in a horizontal layer of fluid, when the higher temperature is on the under side. *Phil. Mag.* **32**, 529–546.

SHAHIN, G.A. & FLORYAN, J.M. 1999 Heat transfer enhancement generated by chimney effect in systems of vertical channels. *Trans. ASME J. Heat Transfer* **121**, 230–232.

SONG, Z., HUANG, X., KUENZER, C., ZHU, H., JIANG, J., PAN, X. & ZHONG, F. 2020 Chimney effect induced by smoldering fire in a U-shaped porous channel: a governing mechanism of the persistent underground coal fires. *Process Saf. Environ. Prot.* **136**, 136–147.

STRAATMAN, A.G., NAYLOR, D., TARASUK, J.D. & FLORYAN, J.M. 1994 Free convection between inclined isothermal plates. *Trans. ASME J. Heat Transfer* **116**, 243–245.

STRAATMAN, A.G., TARASUK, J.D. & FLORYAN, J.M. 1993 Heat transfer enhancement from a vertical, isothermal channel generated by the chimney effect. *Trans. ASME J. Heat Transfer* **115**, 395–402.

TOURNIER, C., GETHON, P. & RABINOWICZ, M. 2000 The onset of natural convection in vertical fault planes: consequences for the thermal regime in crystalline basements and for heat recovery experiments. *Geophys. J. Intl* **140**, 500–508.

WEIL, A. (Ed.) 2012 *Nuclear Power. Practical Aspects*. IntechOpen Book Series.

WONG, N.H. & HERYANTO, S. 2004 The study of active stack effect to enhance natural ventilation using wind tunnel and computational fluid dynamics (CFD) simulations. *Energy Build.* **36**, 668–678.